



Begoña Lavin-Plaza, Alkystis Phinikaridou,
Marcelo E. Andia, Sara Lacerda, Markus Henningsson,
Marcus R. Makowski, and René M. Botnar

Introduction

Cardiovascular disease (CVD) remains the leading cause of death worldwide despite improvements in prevention (e.g., blood pressure control, cholesterol lowering, and smoking cessation) and advances in diagnosis and treatment. Clinical risk scoring systems do not allow satisfactory identification of individuals with subclinical disease and at high risk for coronary events [1, 2]. Coronary artery disease (CAD) and myocardial infarction account for more than 50% of CVD deaths and are the result of atherosclerosis and plaque rupture with subsequent thrombosis. A major challenge of CAD diagnosis is that the majority of patients who die suddenly of CVD have no previous symptoms according to the 2013 AHA statistics [3]. The clinical challenge is that the majority of these plaques do not lead to coronary narrowing and/or ischemia but are characterized by inflammation, increased plaque burden, outward remodeling, spotty calcification, neovascularization, and intraplaque hemorrhage.

Current imaging tests such as X-ray angiography and computed tomography (CT) have failed to identify patients

that are at risk of coronary plaque rupture and subsequent heart attack or stroke [4–6]. Catheter-based imaging techniques such as intravascular ultrasound (IVUS), optical coherence tomography (OCT), and near-infrared spectroscopy (NIRS) allow some limited plaque characterization but are invasive and thus not useful as a screening test [7–9]. Therefore, new noninvasive approaches to detect potentially unstable plaque are urgently needed.

Recent studies with positron emission tomography (PET)/CT and the radiopharmaceuticals ^{18}F -FDG (*inflammation*) [10] and ^{18}F -NaF (*spotty calcification*) [11] have demonstrated the feasibility of coronary plaque imaging with promising results but are beyond the scope of this chapter, and the reader is referred to recent publications [10, 11].

Molecular magnetic resonance imaging (mMRI) using target-specific imaging agents is a noninvasive alternative imaging modality that can provide more accurate information about plaque composition and biology including endothelial dysfunction, inflammation, and vascular remodeling and hemorrhage. Molecular MRI thus may improve the prediction of future coronary events, allow earlier and more aggressive medical treatment, monitor the effectiveness of medical and/or interventional treatment in patients, and may provide novel data on the pathogenesis of atherosclerosis in vivo. Subclinical atherosclerosis may precede the development of clinical disease by many decades, thereby offering the opportunity to use image-guided diagnosis and to target primary prevention therapies to those at highest risk [12].

Studies investigating subclinical and clinical coronary atherosclerosis have included noncontrast-enhanced (NCE) and contrast-enhanced (CE) coronary vessel wall cardiovascular magnetic resonance (CMR). NCE-CMR can identify and quantify early atherosclerotic changes and vascular remodeling [13–17]. Additionally, it can be applied for the detection of intraplaque hemorrhage [18–21], a known marker of plaque instability. Selective visualization of residual coronary thrombus following plaque rupture has been also demonstrated with NCE-CMR [22] and was confirmed by optical coherence tomography (OCT) [23]. Furthermore,

B. Lavin-Plaza (✉) · A. Phinikaridou · S. Lacerda · M. Henningsson
Division of Imaging Sciences and Biomedical Engineering,
King's College London, St Thomas' Hospital, London, UK
e-mail: begona.lavin_plaza@kcl.ac.uk;
alkystis.i.phinikaridou@kcl.ac.uk; sara.lacerda@kcl.ac.uk;
markus.henningsson@kcl.ac.uk

M. E. Andia
Radiology Department, School of Medicine, Pontificia Universidad
Catolica de Chile, Santiago, Chile
e-mail: mandia@med.puc.cl

M. R. Makowski
Department of Radiology, Institut für Radiologie, Berlin, Germany
e-mail: marcus.makowski@charite.de

R. M. Botnar
Division of Imaging Sciences and Biomedical Engineering,
King's College London, St Thomas' Hospital, London, UK
The British Heart Foundation Centre of Excellence, Cardiovascular
Division, King's College London, London, UK

time-resolved bright-blood NCE-CMR in concert with an endothelium-dependent stressor allows assessment of coronary endothelial function, which represents an important predictor for cardiovascular events [18, 24–27]. To gain additional information, CE-CMR can be utilized. Retention of nontargeted contrast agents is associated with the severity of atherosclerosis and the degree of coronary inflammation [28, 29]. The potential of targeted CE-CMR for biological characterization of coronary thrombus and plaque has also been demonstrated in small and large animal models and in humans [30–34].

Pathophysiology of Atherosclerosis

Atherosclerosis is an inflammatory disease that affects medium and large size arteries and usually remains asymptomatic until late-stage disease when plaques enlarge and

reduce arterial blood supply or suddenly rupture, thereby causing thrombotic occlusion and ultimately ischemic events [12, 35] (Fig. 14.1) [36]. It is widely accepted that vascular inflammation is the result of endothelial damage and the subsequent accumulation of low density lipoproteins (LDL) that initiate a complex signalling cascade leading to the recruitment of monocytes and macrophages and the deposition of extracellular matrix (ECM) proteins in the inner layer of the vessel wall [12, 37]. Recent studies have also reported a role of the adventitia [38–40]. Atherosclerosis usually occurs at predilection sites with disturbed laminar flow, such as branch points or at sites with oscillating shear stress [41]. The initial phase is characterized by endothelial dysfunction with structural and molecular alterations, including increasing width of the tight junctions [42, 43] and the activation of cell adhesion molecules, such as intercellular and vascular cell adhesion molecule-1 (ICAM-1 and VCAM-1) and E- and P-selectins [12]. Overexpression of ICAM-1 and VCAM-1 molecules is

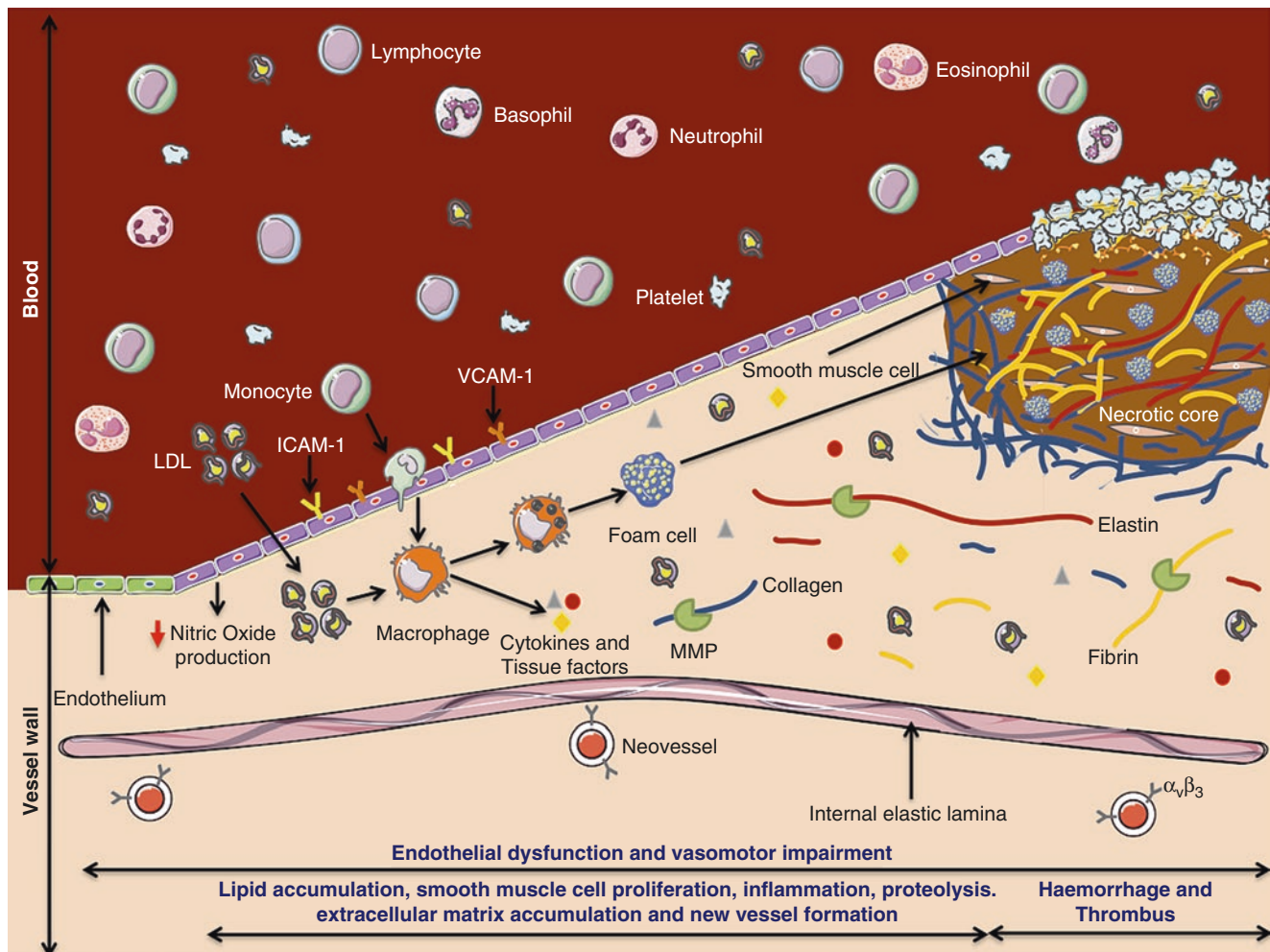


Fig. 14.1 Pathogenesis of atherosclerotic plaque development. Endothelial dysfunction initiates inflammatory processes and leads to the migration of immune cells and LDL into the vessel wall where monocytes differentiate into macrophages which transform themselves with increasing intake of lipids and cholesterol into foam cells. Subsequently, athero-

sclerotic plaques develop which are characterized by activation of platelets and smooth muscle cells, followed by deposition of extracellular connective matrix components and endothelial proliferation and necrotic core formation. (Adapted and reprinted from Springer, © 2014, online, Fig. 1, Lavin et al. [36], © 2014, with kind permission from Springer Nature)

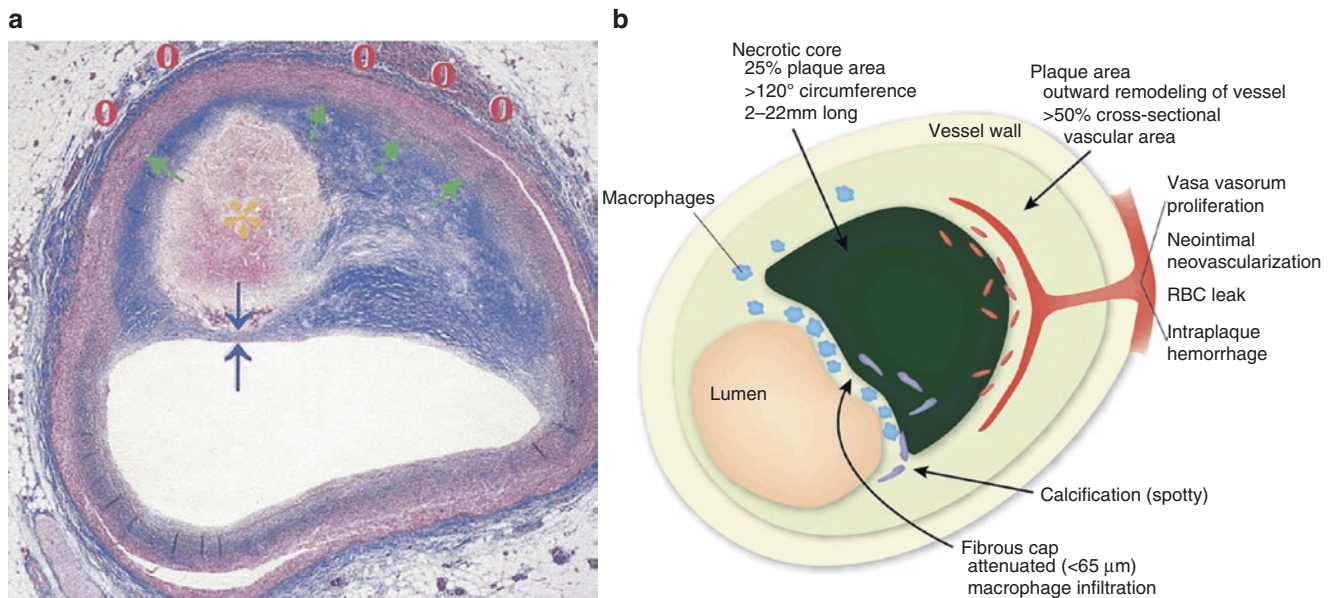


Fig. 14.2 Morphological and biological features of vulnerable plaque. (a) Cross section of a rupture-prone coronary artery plaque with a (1) large lipid-rich necrotic core (orange asterisk), (2) thin fibrous cap (blue arrows), (3) expansive remodeling (green arrow), and (4) vasa vasorum and neovascularization (red circles) [47]. (Adapted and reprinted from

Falk [47], © 2006, with permission from Elsevier). (b) Schematic of a vulnerable plaque highlighting the features associated with plaque instability. (Adapted and reprinted by permission from Narula and Strauss [48], © 2007)

directly related with an increase in monocyte infiltration in the vessel wall where they differentiate into tissue-resident macrophages [44]. Recruitment of immune cells into the artery wall plays a central role in all stages of atherosclerosis. Macrophages uptake oxidized LDL using the scavenger receptors, and as a result of continued intracellular LDL accumulation in macrophages (cytosolic droplets), they transform into foam cells [12, 37]. Subsequent steps include secretion of inflammatory cytokines, activation of platelets, smooth muscle cell proliferation, accumulation of apoptotic cells, and deposition of ECM proteins such as collagen and elastin that collectively contribute to the formation of complex plaque including a necrotic lipid core due to foam cell apoptosis at advanced stages [45]. Alteration and degradation of the ECM by the release of matrix metalloproteinases (MMPs) from macrophages can lead to the progression and destabilization of the plaque [46]. Clinically, the aim is to divide atherosclerotic lesions into low risk (stable plaques) and high risk (vulnerable plaques). Postmortem studies have demonstrated that vulnerable plaques are characterized by a large plaque volume and large necrotic core, low amount of fibrous tissue, accumulation of macrophages, and a thin fibrous cap (Fig. 14.2).

At advanced disease stages, the enlargement of the plaque results in intraplaque hypoxia that triggers additional inflammatory cell infiltration and promotes local neovascularization. Stable plaques are characterized by a thick fibrous cap, high amounts of fibrous tissues, and a small number of macrophages [49, 50].

Cardiovascular Imaging

Cardiac MRI has become a clinically accepted imaging modality for assessment of left ventricular morphology and function, myocardial perfusion, viability, and tissue characterization including the measurement of diffuse myocardial fibrosis [51–55]. Due to ongoing technical advances in MR acquisition and reconstruction and contrast agent development, coronary MRI and vessel wall imaging are an emerging noninvasive imaging technique for comprehensive coronary assessment. Compared to other clinical imaging modalities such as single-photon emission computed tomography (SPECT) and position emission tomography computed tomography (PET/CT), MRI provides high spatial and temporal resolution allowing for a comprehensive cardiac evaluation including morphology, function, perfusion, and myocardial tissue characterization [51–55]. The development of novel plaque-specific MR contrast agents also allows imaging of biological processes in the vessel wall without exposure of the patient to harmful ionizing radiation or iodinated contrast agents.

MRI is based on the nuclear magnetic properties of atoms (mainly hydrogen) and involves the interplay of three components to generate tomographic images: the main magnetic field of the scanner (static magnetic field) which generates a net magnetization along the scanner axis, the gradient fields which are used for spatial localization, and the oscillating magnetic field of the radio-frequency (RF) pulses. RF pulses

are used to change the orientation of the magnetization, inducing excitation of the water protons. Following the RF pulse excitation, protons return to their equilibrium stage, and specific receiver coils detect the energy emitted during this relaxation. The most important proton properties used by MRI are the proton density and two characteristic relaxation times called spin-lattice relaxation time and spin-spin relaxation time, denoted as T_1 and T_2 , respectively. Signal intensity primarily depends on the local values of R_1 ($1/T_1$) and R_2 ($1/T_2$) relaxation rate of water protons [56]. Considering the relatively low sensitivity of MRI, the use of specific contrast agents aids the detection of differences between pathological and normal surrounding tissues. For that, local concentrations of a contrast agent are needed to alter the relaxation rate of water protons sufficiently for detectable signal effects. An important consideration to take into account during vessel wall imaging is the distribution of the contrast agent in non-targeted regions and the adjacent blood pool. In some cases, to distinguish between the luminal area and the vessel wall contrast uptake, it might be necessary to wait for the contrast agent to clear sufficiently from the blood.

Imaging Sequences

Vessel wall MRI can be achieved without contrast agents by exploiting the ability of MRI to suppress signal from adjacent tissues which mainly include luminal blood and

epicardial fat. Fat suppression is commonly performed using spectrally selective inversion magnetization preparation pulses, where the image acquisition is timed to coincide with the nulling point of the fat signal. Alternatively, signal from fat can be minimized using water-selective RF pulses for imaging [57] or using the DIXON water-fat separation technique [58, 59]. To suppress blood signal (so-called black-blood MRI), traditionally, flow-dependent techniques have been employed such as double inversion recovery (DIR) [60, 61]. However, DIR is typically limited to two-dimensional cross-sectional imaging of the vessel wall or requires local inversion pulses for three-dimensional coronary vessel wall imaging [62] (Fig. 14.3). More recently, motion-sensitized driven equilibrium (MSDE) [63], delay altering with nutation for tailored excitation (DANTE) [64], and variable flip-angle turbo spin echo with flow-sensitive dephasing have been proposed to allow for flow-dependent three-dimensional coverage [65]. Such volumetric coverage is desirable due to the long and tortuous geometry of the coronary arteries and simplifies MRI scan planning compared to DIR. A schematic overview of a ECG-triggered black-blood imaging sequence is provided in Fig. 14.4. Blood signal suppression can also be achieved using flow-independent techniques which typically rely on the difference in T_1 or T_2 between vessel wall, thrombus, and blood [19, 21, 27, 66, 67] or a combination of T_2 and T_1 [65, 68] (Fig. 14.5).

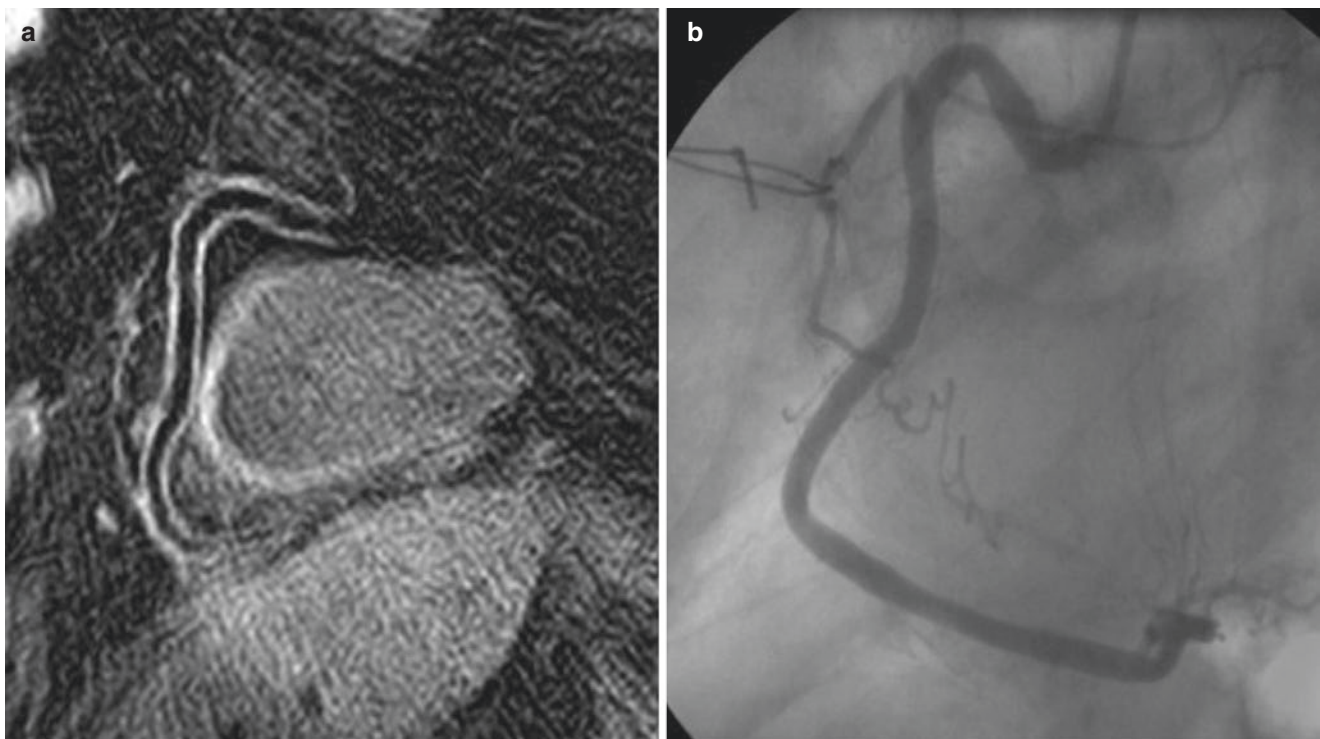


Fig. 14.3 Local inversion black-blood coronary wall imaging for the quantification coronary arterial remodeling and plaque burden. (a) 3D black-blood vessel wall image of the right coronary artery wall (RCA)

in a patient with nonsignificant coronary artery disease on X-ray coronary angiography. (b) Vessel wall images demonstrate some minor wall thickening in the proximal and mid RCA segment

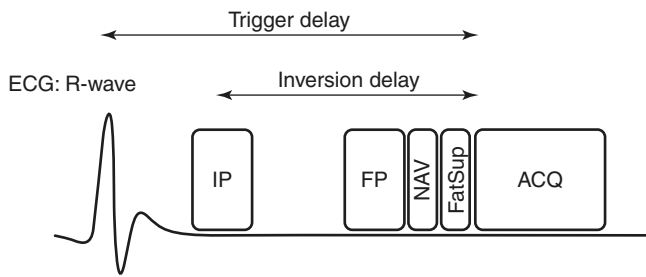


Fig. 14.4 Generic black-blood vessel wall MRI pulse sequence. Cardiac motion is compensated for by synchronizing the image acquisition (ACQ) with an electrocardiogram (ECG) and using a trigger delay from the R-wave to time ACQ to mid-diastole. Respiratory motion compensation can be performed using respiratory navigation (NAV) which typically precedes ACQ. Fat suppression is performed prior to ACQ using a fat-selective RF pulse to null the fat signal. Black-blood contrast can be achieved either with inversion preparation (IP) where an inversion delay is used to null signal from the blood or alternatively using flow preparation (FP) where signal from flowing blood is destroyed using dephasing gradients or a combination of small RF pulses and gradients. (Adapted and reprinted from Springer, © 2014, online, Fig. 2, Lavin et al. [36], © 2014, with kind permission from Springer Nature)

Flow independence overcomes the problem of inadequate blood suppression in the case of slow laminar flow and facilitates volumetric whole-heart coverage (Fig. 14.6).

Vessel wall MRI can also be performed using contrast agents, either with T1-shortening gadolinium-based agents or T2/T2* shortening iron-based agents. Contrast agent quantification is then typically done using T1 and T2/T2* mapping sequences of which several implementations exist. The most commonly used T1 mapping sequences are the Look Locker (Fig. 14.7), the modified Look Locker inversion recovery (MOLLI) [69], and the saturation recovery single-shot acquisition (SASHA) [70] sequence and combinations of it [71]. T2 and T2* mapping is typically done with a multi-echo spin-echo and gradient-echo (Fig. 14.8) technique, respectively. Recent implementations also include the use of T2 prep pulses with varying echo times for cardiac T2 mapping [72–74].

An important requirement for coronary vessel wall visualization is high spatial resolution. Although improved spatial resolution can be achieved with the use of dedicated

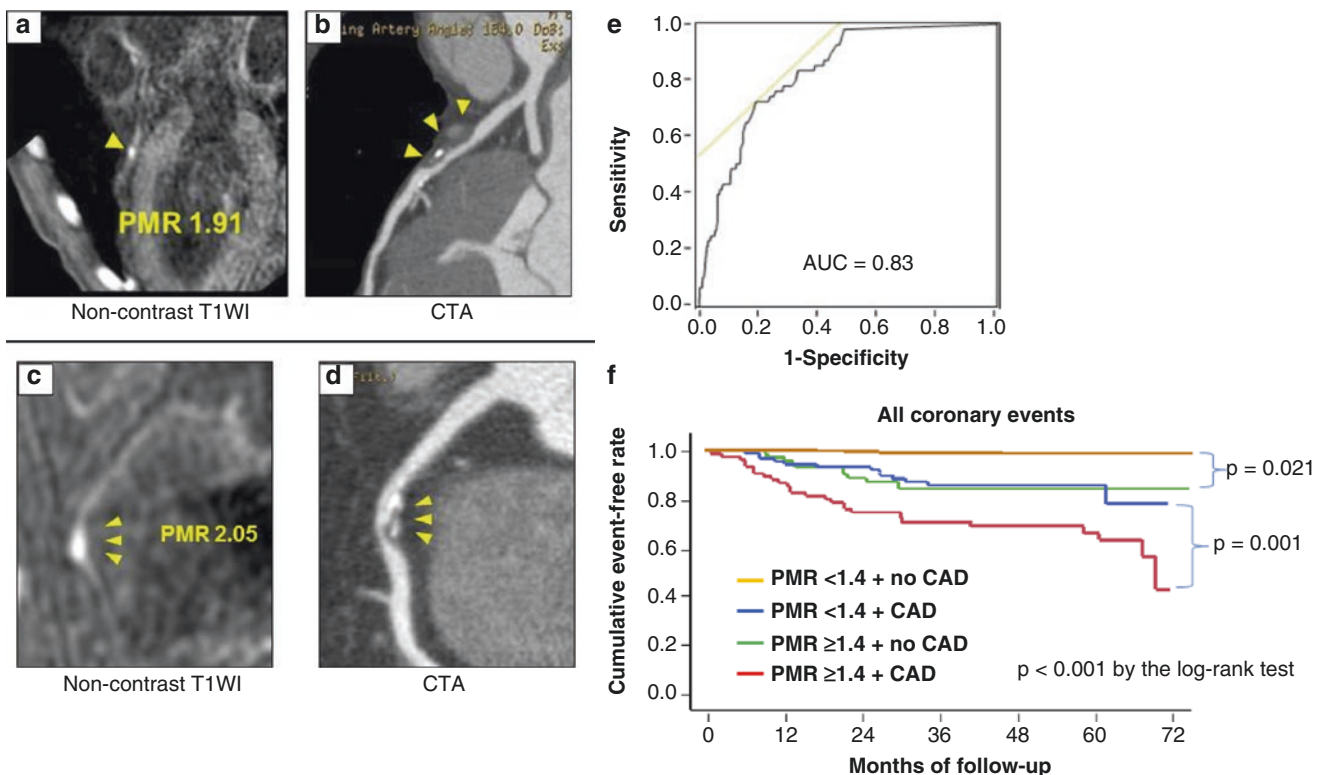


Fig. 14.5 Representative images of HIPs with PMRs ≥ 1.4 . Representative noncontrast T1-weighted images of high-intensity plaques (HIPs) (yellow arrowheads) in the proximal left anterior descending coronary artery (a) and the right coronary artery (c), in which plaque-to-myocardium signal intensity ratios (PMRs) were 1.91 and 2.05, respectively. These high-intensity signals each correspond to the left and right coronary plaques on computed tomographic angiography (CTA) (yellow arrowheads on curved multiplanar reformation images), (b) and (d). T1WI = T1-weighted imaging. (e) ROC Curve Analysis for Developing Coronary Events and Flowchart of Study Patients on the Basis of PMR. From receiver-operating characteristic (ROC) curve analysis, a plaque-to-myocardium signal intensity ratio

(PMR) of 1.4 was identified as the best cutoff value for predicting cardiac events, with 69.5% sensitivity and 82.3% specificity. The calculated area under the curve (AUC) was 0.83. (f) Kaplan-Meier curves comparing the probability of all coronary events. Coronary event-free survival was worst in the group with plaque-to-myocardium signal intensity ratios (PMRs) ≥ 1.4 and coronary artery disease (CAD) (red line) and best in the group with PMRs < 1.4 but no CAD group (orange line). The rate in the group with PMRs ≥ 1.4 and no CAD (green line) was intermediate but comparable with that in the group with PMRs < 1.4 and CAD (blue line) (Adapted and reprinted from, Noguchi et al. [19], © 2014, with permission from Elsevier)

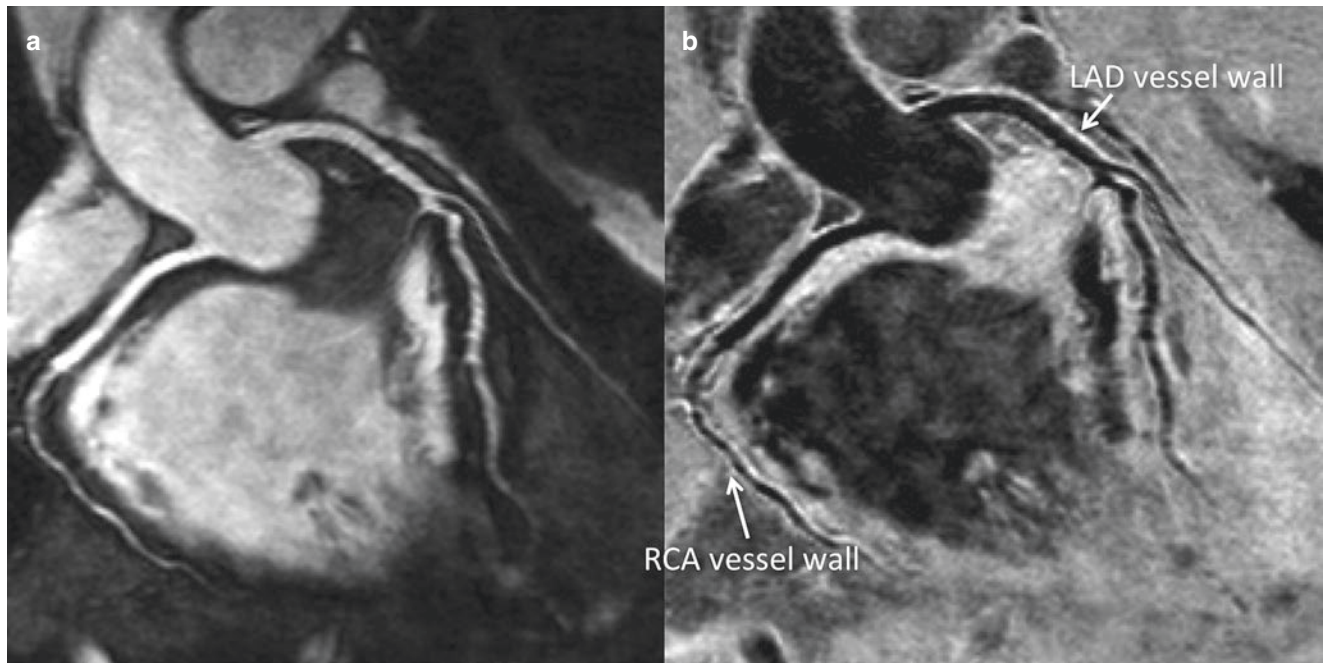


Fig. 14.6 Flow-independent 3D whole heart coronary vessel wall imaging using an interleaved T2 prep imaging sequence. (a) 3D bright-blood SSSFP coronary artery image in a healthy volunteer without history of coronary artery disease demonstrating normal left and right coronary arteries. (b) Corresponding whole heart vessel wall image

clearly delineates the coronary vessel wall both in the proximal and distal segments due to the flow-insensitive nature of the iT2 prep imaging sequence. (Adapted from, Andia et al. [67], © 2012, with permission of John Wiley and Sons)

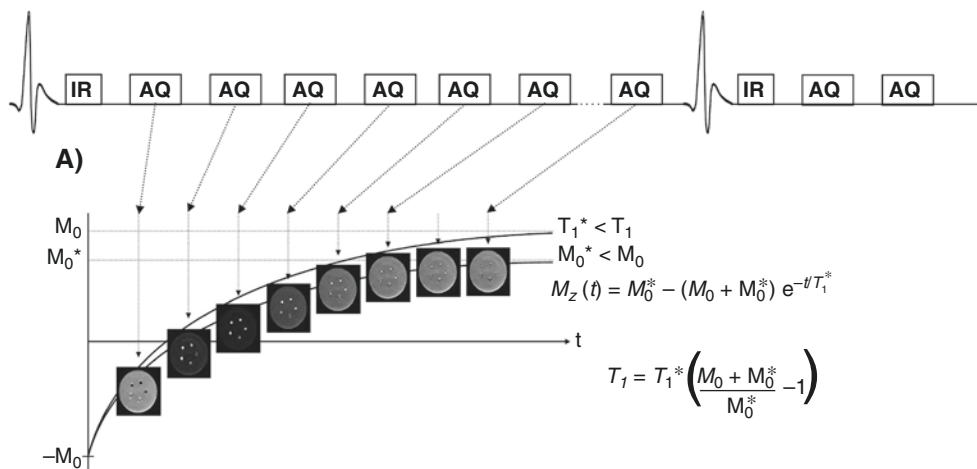


Fig. 14.7 Schematic of inversion recovery Look Locker (LL) T_1 mapping sequence. The inversion pulse precedes the imaging sequence (AQ), which allows pixel-wise sampling of the recovery of the M_z magnetization of, e.g., tissues, fluids, or blood. A least square fit of the measured M_z values to the Bloch equation allows pixel-wise estimation of

T_1 and estimation of the local contrast agent concentration $[Gd^{3+}]$. A T_1 correction is usually performed as the repetitive use of RF pulses alters the recovery of the M_z magnetization leading to a lower value for the steady-state magnetization, $M_0^* < M_0$, and thus to a shorter value for the relaxation time $T_1^* < T_1$

multichannel cardiac receiver coils, coronary vessel wall imaging is challenging due to the slow acquisition speed of MRI relative to the physiological motion. This includes both cardiac and respiratory motions, which are both one order of magnitude larger than the achievable spatial resolution. However, to mitigate the effects of motion, which include

image blurring and ghosting, cardiac and respiratory motion compensation methods have been introduced. Cardiac motion can be effectively minimized by synchronizing the MRI scanner with an electrocardiogram (ECG) and limit the data acquisition to the most quiescent cardiac phase. Although the timing and duration of the cardiac rest period is

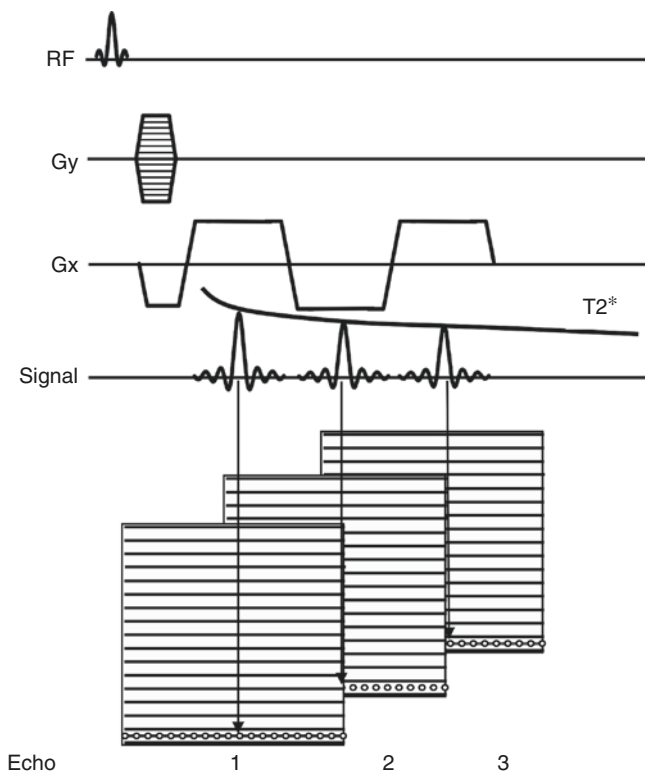


Fig. 14.8 Schematic of T_2^* mapping sequence using Cartesian k-space sampling. Acquisition of multiple echoes allows sampling the T_2^* decay envelope and thus to estimate the T_2^* relaxation time of tissues and blood

subject and heart rate dependent, time-resolved MRI cine scans can be used to identify the most suitable acquisition window. For respiratory motion compensation, a so-called respiratory navigator can be used. Conventional respiratory navigator techniques involve measuring the displacement of the lung-liver interface in feet-head direction and only accept data acquired within a narrow “gating window,” typically defined around end-expiration. Furthermore the measured navigator position can be used to update the MR image in real time based on a motion model which is often assumed to be a linear relationship of 0.6. A drawback of this approach is that the scan time is prolonged because a large portion of the data falls outside the gating window and has to be remeasured (typically only 20–50% is inside the window), as well as the indirect motion measurement requiring a motion model. Recently, technical advances have allowed for direct measurement of respiratory induced motion using self-gating or image navigators, which directly measure the respiratory motion of the heart which and thus obviate the need for a gating window and reduce scan time [57]. Currently, several flavors exist which include beat-to-beat [75, 76] or bin-to-bin [77, 78] motion correction or a combination of it [79, 80]. These techniques now allow correcting for respiratory motion in two or three dimensions and to apply more sophisticated motion correction algorithms including affine and

nonrigid transformations and also integrating motion correction directly into image reconstruction [77]. Latest developments do not require neither ECG synchronization nor respiratory gating and acquire data continuously throughout the cardiac cycle [81, 82]. Data are typically acquired with the golden angle approach and a 3D radial trajectory with repetitive acquisition of the center k-space line in foot-head (FH) direction. The self-gating signal allows estimation of both the ECG and the respiratory signal using principal component analysis and thus to retrospectively sort the cardiac phases and to perform respiratory binning. These 4D datasets allow selecting the cardiac phase with best vessel lumen and wall visualization.

T1 Contrast Agents

The most commonly used contrast agents are based on gadolinium (Gd) complexes that lead to positive contrast detected as a local increase in MRI signal intensity or brightness [83]. Gd(III) is a metallic element with seven symmetrical, unpaired electrons characterized by a strong paramagnetic susceptibility, which produces a slow electron spin relaxation rate that significantly affects the surrounding water protons. Therefore, it has the effect of shortening T_1 relaxation time in tissues where it accumulates, enhancing the signal in post-contrast T_1 -weighted images. Following Gd(III) administration, they rapidly distribute into the extracellular fluid space. Subsequently, they are then gradually excreted via the kidneys with a 60–90 min half-life for most small molecular weight agents (~1000 Da) in patients with normal renal function and completely eliminated after 24 h [83]. Due to its toxicity, Gd(III) must be chelated for in vivo application. Several chelating approaches have been published with cyclic chelates (DOTA) demonstrating better metabolic stability than linear chelates (DTPA) [84]. Another important aspect is the optimization of the relaxivity properties of these Gd(III) complexes to improve signal enhancement and therefore the sensitivity of these imaging agents. For protein- or cell-specific imaging, targeting moieties have been attached to Gd(III) chelates to allow the evaluation of molecular or cellular changes associated with different disease stages. The relaxivity of gadolinium chelates is dependent on several parameters such as molecular motion and water exchange [83] (Fig. 14.9).

A good example of the impact of these two parameters on relaxivity is the Gd-DTPA analog gadofosveset trisodium, Ablavar (Lantheus Medical Imaging, North Billerica, USA), which binds to human serum albumin and increases its relaxivity by five-fold compared to the unbound fraction [86]. This effect is known as receptor-induced magnetization enhancement (RIME) [87] and has been exploited for other protein-binding imaging agents including the elastin-binding contrast agent (ESMA) [88] or a fibrin-binding contrast agent,

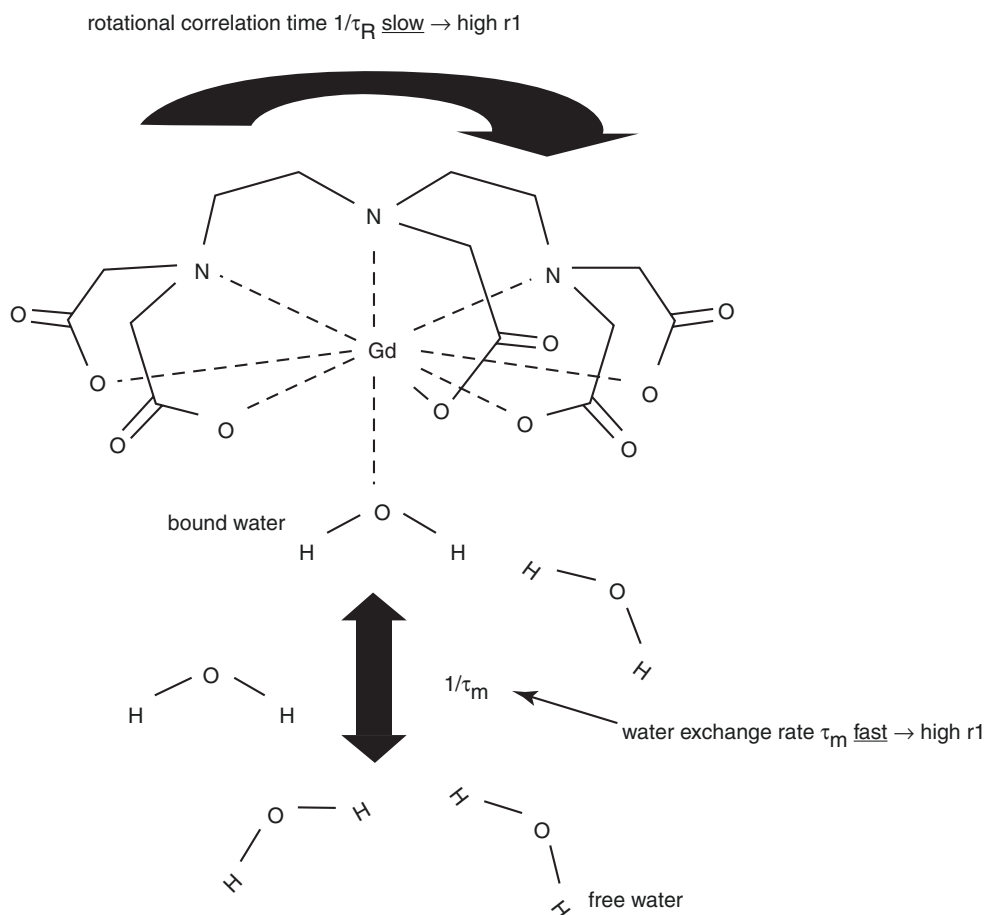


Fig. 14.9 Schematic of water exchange between bound and free water of a gadolinium chelate. The proton bound to gadolinium exchanges its magnetic properties with the free water leading to a shortening of T_1 in the vicinity of the contrast agent. Fast water exchange leads to a more efficient energy transfer between gadolinium and free water, thereby creating a higher relaxivity r_1 . The amount of T_1 shortening is given by the relaxivity (r_1) of the contrast agent, which depends on the number of bound protons, the water exchange rate ($1/\tau_m$), and the T_1 relaxation

time of bound water (T_{1m}). T_{1m} itself depends on several factors including the distance to the gadolinium atom and the rotational correlation time ($1/\tau_r$). Upon binding to a large protein or cell, $1/\tau_r$ significantly decreases thereby increasing r_1 and thus increasing the T_1 -shortening effect of the contrast agent. Construction of macromolecular agents (e.g., dendrimers) is another means of slowing down the rotational motion of Gd compounds. (Adapted from Caravan [85])

EP-2104R [89]. Other approaches to improve r_1 relaxivity is the use of lipid-perfluorocarbon emulsions that allow increasing the number of Gd(III) atoms per probe. A good example of these lipid-perfluorocarbon emulsions is a fibrin-specific contrast agent where multiple Gd(III) atoms were targeted with biotin that can bind to avidin derivatized with an antibody to recognize fibrin (present in the clot) [90]. Another approach is the use of a lipid tail to increase the number of Gd(III) per molecule. A contrast agent that detects angiogenesis by $\alpha v\beta 3$ -targeting is an example of this design [91].

T2 and T2* Contrast Agents

Although Gd(III)-based contrast agents usually increase $1/T_1$ and $1/T_2$ (R_1 and R_2 , respectively) in similar amounts [85, 92, 93], it is well established that iron particle-based con-

trast agents have a much stronger effect on increasing R_2 [94]. The paramagnetic properties of iron particles usually disturb the surrounding magnetic field causing a negative contrast effect detected as a decrease of signal intensity or darkness. This effect can be accurately detected with T2- and T2*-weighted imaging sequences. Moreover, it has also been demonstrated that iron-based particles can provide higher sensitivity in target detection compared to gadolinium-based contrast agents [95]. Depending on the size range of these particles, they can be divided into micron-sized iron oxide particles (MPIO) $\approx 10 \mu\text{m}$ in diameter, monocrystalline iron oxide particles (MION) $\approx 3 \text{ nm}$ in diameter, ultrasmall superparamagnetic iron oxide particles (USPIO) $\approx 15\text{--}30 \text{ nm}$, and superparamagnetic iron oxide particles (SPIO) $\approx 60\text{--}180 \text{ nm}$. SPIOs have an iron oxide core that is stabilized with a monomer or polymer coating. SPIOs are characterized by good suspensibility, uniform

particle size distribution, highly reactive surface, and the possibility of coating modifications to attach specific ligands for biomedical applications. The size and surface properties (in particular charge) have a decisive influence on the elimination, cell response, and toxicity. The maximum effect of SPIO in tissue is usually detected 24–48 h after administration [96]. The non-specific uptake of SPIOs by the mononuclear phagocyte system after intravenous administration is well established. This process allows the use of SPIOs in both to image organs, in particular the liver, spleen, lymph nodes, and bone marrow [97]. One of the major drawbacks of iron-containing particles due to the non-specific uptake by mononuclear phagocytes is the short blood half-life that limits their application in MRI. In order to increase the blood half-life of these particles, several approaches have been implemented, of which modifying the probe coating and decreasing their hydrodynamic diameter (e.g., USPIO) are the most frequent. USPIOs are iron oxide nanoparticles composed of Fe_2O_3 and Fe_3O_4 stabilized by different coating agents. USPIOs are predominantly used for molecular imaging of atherosclerosis [98], myocardial infarction [99], and cancer [100]. Various studies have demonstrated the possibility to identify carotid plaque inflammation noninvasively using USPIOs in both animals and human [101–104]. The use of USPIO particles has allowed the direct visualization of macrophage infiltration in carotid atheroma in vivo [105, 106]. Additionally, USPIOs have a high r_1 , which produces an increase in signal intensity using T1-weighted sequences. At low USPIO concentrations, a T₁-enhancing effect can be observed, whereas at higher doses, the susceptibility phenomenon balances the T₁ effect (nonlinearity in the signal-concentration relationship). Thus, according to the sequence and the local concentration of USPIO, T₁-, T₂-, and T₂*-enhancing effects can be observed independently. In this regard, USPIOs can also be used for T1-weighted imaging to acquire angiograms of the coronary arteries, carotid arteries, and aorta.

Contrast Agents

Endothelial Dysfunction

During the first stages of atherosclerosis, the endothelium develops several functional alterations due to cardiovascular risk factors such as smoking, diabetes, hypercholesterolemia, and obesity, a condition known as endothelial dysfunction [42]. Under these circumstances, endothelial cells are characterized by a reduction in the net production of nitric oxide (NO), leading to impaired vasodilation and an increase in endothelial permeability that allows the influx of LDL and inflammatory cells into the vessel wall [12]. Additionally, endothelial cells increase the expression of

surface-specific adhesion molecules such as VCAM-1, ICAM-1, and E- and P-selectins that contribute to the adhesion and infiltration of immune cells into the vessel wall [12]. Several studies have observed a correlation between endothelial dysfunction and plaque burden, representing an interesting imaging target [24]. Gadofosveset is a clinically approved contrast agent with a long blood half-life time due to binding to human serum albumin and thus ideally suited for MR angiography [85, 86]. Recent studies by our group have demonstrated the ability of gadofosveset to detect changes in endothelial permeability in the brachiocephalic artery of atherosclerotic ApoE^{-/-} mice [107] (Fig. 14.10) and for monitoring effectiveness of interventions in retarding plaque progression [108].

Gadofosveset enhancement has been also correlated with leaky neovessels in atherosclerotic rabbits [110], stent-induced coronary injury in swine [111], and patients with carotid artery disease [109]. Endothelial adhesion molecules are highly expressed in the early stages of atherosclerosis, and therefore different approaches have been developed to specifically image those molecules. In vivo imaging of atherosclerotic plaque has been successfully performed in ApoE^{-/-} mice using VCAM-1-specific nanoparticles [112, 113].

Hypoxia: Angiogenesis and Apoptosis

During the progression of atherosclerosis, the size and composition of the vessel wall changes and local hypoxic areas can contribute to the generation of new vessels, a process known as angiogenesis [114]. This process plays a central role in plaque enlargement and disease progression, and the density of neovessels has been linked with vulnerable or unstable plaques [115]. Gadofosveset has been successfully used to image neovessel-rich areas in different animal models and patients [109, 116, 117]. In contrast to healthy tissues, endothelial cells of immature neovessels are activated and express the surface marker $\alpha_v\beta_3$ in significant amounts [118, 119]. It has been demonstrated that $\alpha_v\beta_3$ -targeted paramagnetic nanoparticles allow the noninvasive assessment of $\alpha_v\beta_3$ -integrin expression in the aortic wall of hyperlipidemic rabbits during the first stages of atherosclerosis [91]. Alternative approaches include the use of dynamic contrast-enhanced T1-weighted MR imaging using clinically approved contrast agents such as gadopentetate dimeglumine [120].

Hypoxic conditions can also lead to the apoptosis of immune cells which has been described as another marker of plaque instability [121]. During apoptosis, cells express specific surface markers like annexin 5 or caspases [122]. An annexin A5-functionalized micellar contrast agent has been successfully used to image apoptosis in atherosclerotic ApoE^{-/-} mice [123]. Moreover, a novel caspase-3/7-

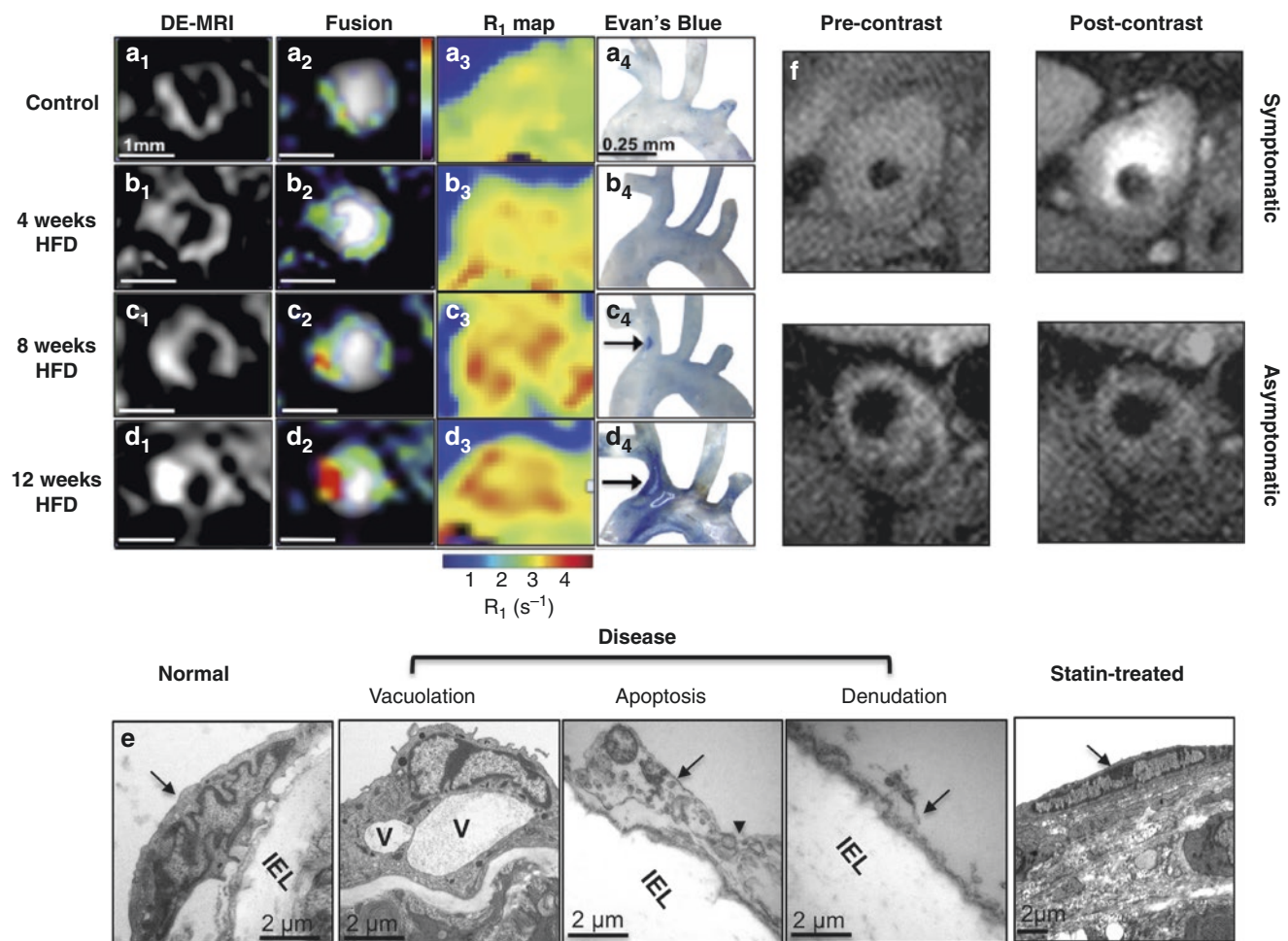


Fig. 14.10 Uptake of an albumin-binding MR contrast agent correlates with endothelial permeability and plaque progression. Late gadolinium enhancement (LGE) MRI and T_1 mapping of endothelial permeability throughout the course of plaque development in high-fat diet (HFD)-fed apoE^{-/-} mice using an albumin-binding contrast agent, gadofosveset, (**a₁–d₁**) and (**a₃–d₃**). Evan's blue dye staining of the aortic arch and brachiocephalic artery shows good agreement (**a₄–d₄**). TEM of endothelial cell (EC) morphology (**e**) showed gradual disease development starting with vacuolation and almost complete EC denudation

after 12 weeks of HFD and normalization in mice treated with statins Fig. 14.10a–e. (Adapted and reprinted from, Phinikaridou et al. [107], © 2012, with permission from Wolters Kluwer Health). Clinical data (**f**) demonstrate increased gadofosveset uptake in patients with symptomatic carotid artery disease, which correlated with increased neovessel density and macrophage count Fig. 14.10f. (Adapted and reprinted from, Lobbes et al. [109], © 2010, with permission from Wolters Kluwer Health)

activatable Gd-based probe (C-SNAM) has been successfully used to image apoptosis in experimental mouse tumor models [124].

Macrophages

During the progression of atherosclerosis, there is a constant influx of immune cells into the vessel wall. The most prominent immune cells that invade these lesions are monocytes that differentiate into plaque resident macrophages where they uptake large amounts of cholesterol to generate so-called foam cells filled with numerous cholesterol ester droplets [12]. Macrophages can alter their phenotype and

function in response to the local microenvironment also known as macrophage polarization [125]. In this regard, there is evidence suggesting that different stages of atherosclerosis are associated with distinct macrophage subtypes, M1, classically activated or pro-inflammatory macrophages, and M2, alternatively activated or resolving macrophages [125]. Although different strategies have been developed to target monocytes, none of them has had the ability to distinguish between macrophage subtypes. Thus, the development of an M1- or M2-specific probe remains an interesting challenge. The phagocytic properties of macrophages have been used for the passive targeting using different types of iron particles in both animal models [103, 126–131] and humans [97, 104, 132–135] (Fig. 14.11).

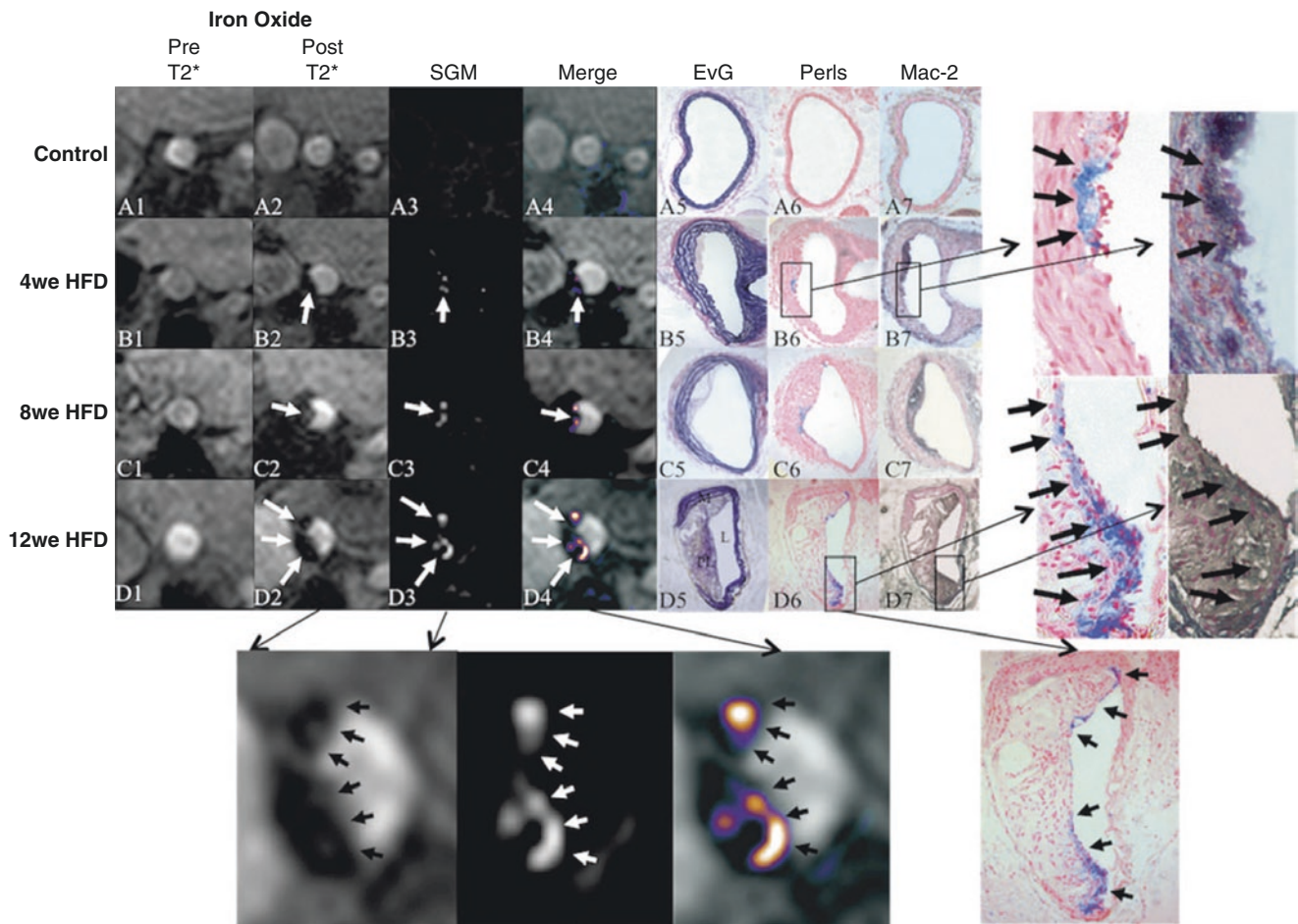


Fig. 14.11 In vivo imaging of macrophages in the brachiocephalic artery of apoE mice on HFD. Bright-blood imaging was performed such that a 2D slice was obtained perpendicular through the brachiocephalic artery (**a**₁₋₂, **b**₁₋₂, **c**₁₋₂, and **d**₁₋₂). SGM-positive contrast images were derived and merged with the bright-blood images (**a**₃₋₄, **b**₃₋₄, **c**₃₋₄, and **d**₃₋₄). Representative images after the injection of the iron oxide agent from control as well as mice on the HFD for 4, 8, and 12 weeks and corresponding elastica van Gieson stain, Perls stain, and immuno-

histochemical analysis for Mac-2 (macrophage marker). Contiguous histological sections were taken in a similar orientation as the in vivo MRI of the brachiocephalic artery. Perls staining was used to demonstrate colocalization of iron-positive areas (**a**₆, **b**₆, **c**₆, and **d**₆) with Mac-2-positive (**a**₇, **b**₇, **c**₇, and **d**₇) (M indicates media, PI plaque, and L lumen). HFD high-fat diet. (Adapted and reprinted from, Makowski et al. [131], © 2011, with permission from Wolters Kluwer Health)

An alternative to non-specific nanoparticles are receptor-specific probes. The scavenger receptors are macrophage-specific surface proteins that are significantly overexpressed on activated macrophages and foam cells, but not expressed on other cells [102]. With the use of gadolinium, immunomicelles targeted to the macrophage scavenger receptor CD206-activated macrophages have been successfully imaged in atherosclerotic plaque of ApoE^{-/-} mice [102]. An alternative approach for macrophage imaging has been developed using gadolinium-loaded LDL-based nanoparticles and modified HDL nanoparticles. Fluorine-containing nanoparticles are avidly taken up by macrophages and therefore can be used to quantify the recruitment of inflammatory cells into atherosclerotic lesions. Since fluorine is absent in the human body, the measurement of fluorine uptake offers a unique possibility to directly detect and

quantify the temporal and spatial evolution of the inflammatory response. In vivo imaging of cardiac and cerebral ischemia has been successfully performed in mice using this approach [136].

Lipids

Uptake of lipids into the vessel wall is one of the processes present throughout the development of atherosclerosis [12, 125]. There is a strong relationship between high serum lipid levels, especially of low-density lipoproteins (LDL), and coronary risk [137]. Since oxidized LDL is one of the drivers of vessel wall inflammation, it represents an interesting imaging target. Gadofluorine M is a gadolinium-based contrast agent that has been successfully used to image increased

neovascularization in advanced lipid-rich atherosclerotic lesions in rabbits [138]. Moreover, the incorporation of an apoE-derived lipopeptide (P2fA2) into the lipid layer of HDL nanoparticles (rHDL-P2A2) has been developed as a platform for molecular MRI of macrophages in atherosclerotic plaques in vivo [139].

Extracellular Plaque Components and Proteolytic Enzymes

Another approach to noninvasively image atherosclerosis is targeting extracellular plaque components. The extracellular matrix is a protein- and carbohydrate-based lattice. In atherosclerotic vessels, smooth muscle cells and macrophages increase the synthesis and secretion of ECM components such as collagen and elastin, and this turnover is related with

vascular wall remodeling [140]. To detect the alteration of the ECM under pathological conditions, a small molecular weight elastin-specific gadolinium-based contrast agent (ESMA) has been developed. The ability of ESMA to detect plaque burden and ECM remodeling has been demonstrated at different stages of atherosclerosis in a murine model and in a porcine model of coronary injury [32, 141] (Figs. 14.12 and 14.13).

In addition to quantifying the plaque burden using the ESMA, a study using a rabbit model of experimentally induced thrombosis allowed in vivo classification of vascular remodeling in negative, intermediate, and positive for the detection of “high-risk/vulnerable” plaque [142] (Fig. 14.14).

Similarly, to prospective clinical studies in humans with coronary artery disease [49, 143, 144], the rabbit study showed that positive remodeling measured after administration of ESMA was associated with plaque instability.

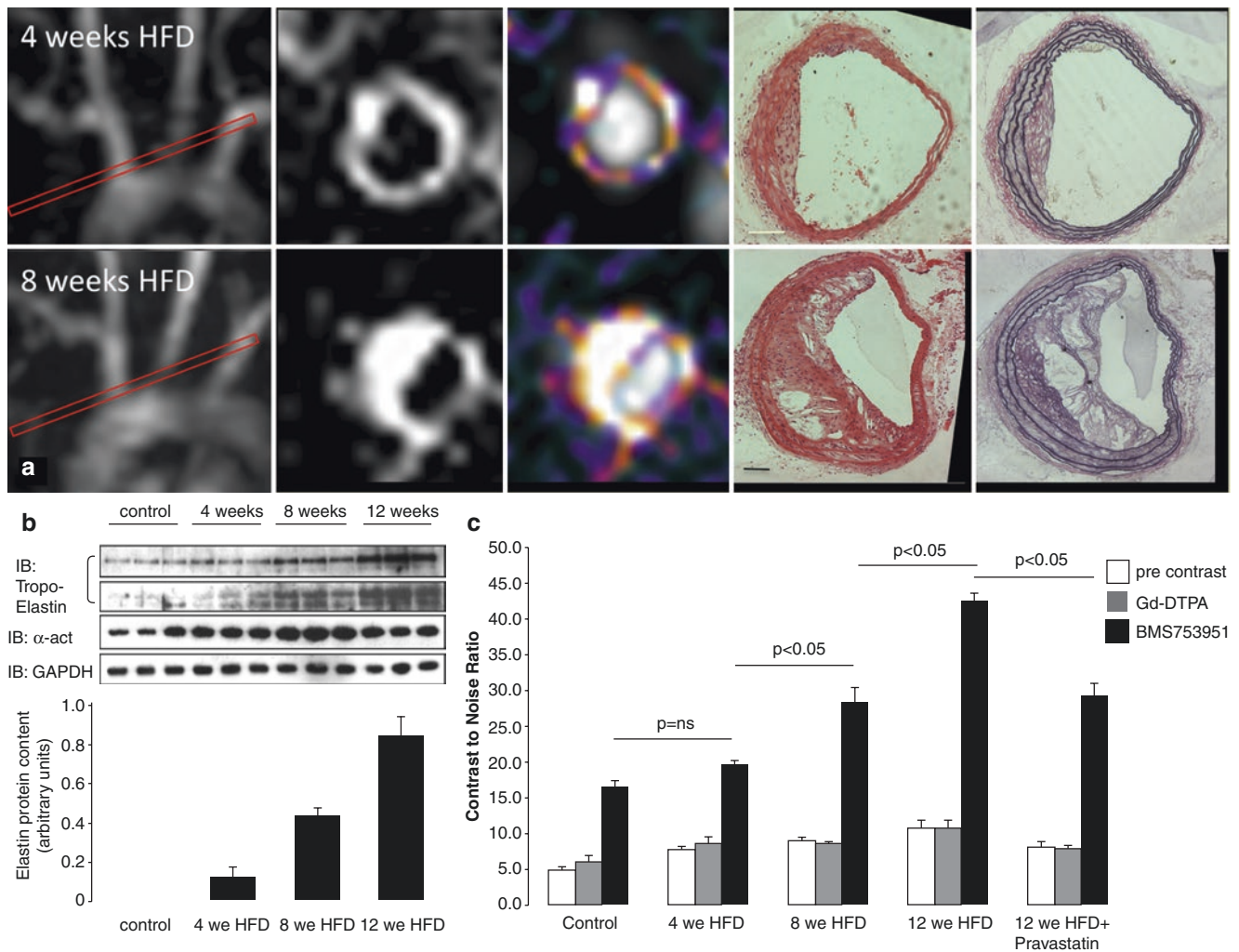


Fig. 14.12 MRI of extracellular matrix remodeling in an apoE^{-/-} mouse model of accelerated atherosclerosis at 4 and 8 weeks after commencement of HFD using an elastin-specific MR contrast agent (a), ESMA (Lantheus Medical Systems, North Billerica, MA, USA).

(b) Tropoelastin content as measured by Western blotting increased with the duration of the HFD, which was paralleled by an increased contrast-to-noise values after ESMA injection (c) (Adapted from Makowski [88])

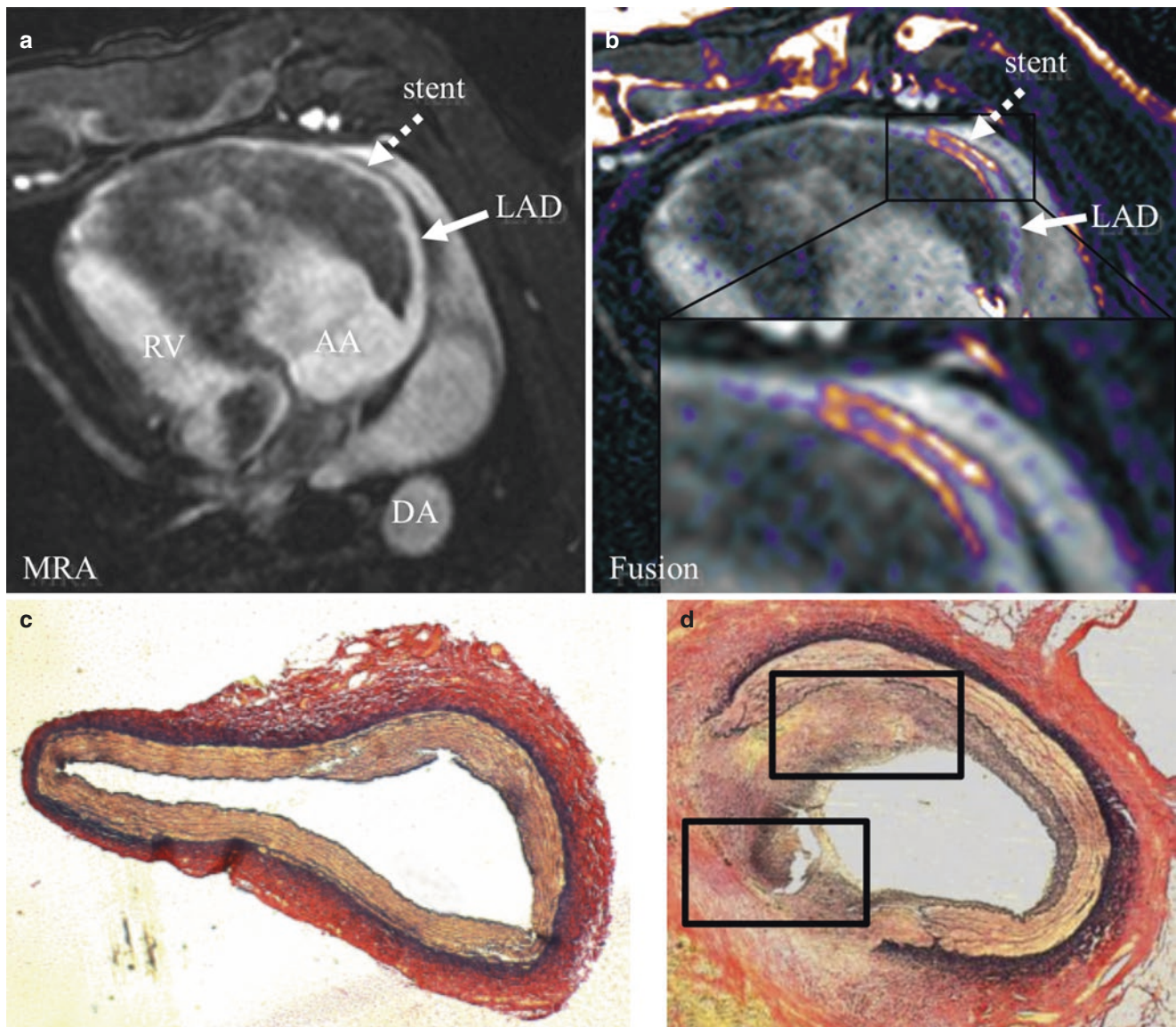


Fig. 14.13 Elastin imaging of coronary remodeling. Comparison of coronary MRA (a), delayed-enhancement MRI (b), and positron-emission CT-like fusion of a and b (c) of stented and control coronary vessel segments and corresponding histology (d) and (e). Strong enhancement can be observed at the stent location (dotted white arrow), whereas little to no enhancement is visible in the normal noninjured left anterior descending artery segment (b) and (c). Elastica van Gieson

stain of noninjured coronary vessel segment (d) shows intact internal elastic lamina (IEL) and circular arranged elastin fibers (black) in the media. Elastica van Gieson of stented vessel segment (e) demonstrates disruption of IEL and neointima formation with diffuse elastin deposition (black dots). (Adapted and reprinted from, von Bary et al. [32], © 2011, with permission from Wolters Kluwer Health)

An alternative to directly imaging the ECM is to target proteolytic enzymes that are implicated in the degradation of ECM components such as collagen and elastin [140, 145]. These enzymes are mainly secreted by macrophages and are known as matrix metalloproteinases or MMPs. MMPs have been linked to plaque instability [145]. Noninvasive imaging of MMPs has been successfully performed using a gadolinium chelate targeted to a MMP inhibitor (P947) in murine

and rabbit experimental models [146, 147]. Moreover, the enzyme myeloperoxidase (MPO) has been used as an emerging biomarker of plaque instability and future acute events [148]. It has also been demonstrated the feasibility of a specific gadolinium-based probe that targets MPO-Gd to image atherosclerosis in hyperlipidemic rabbits [149]. In addition, MPO-Gd enhancement colocalizes with plaque areas rich in infiltrated macrophages [149].

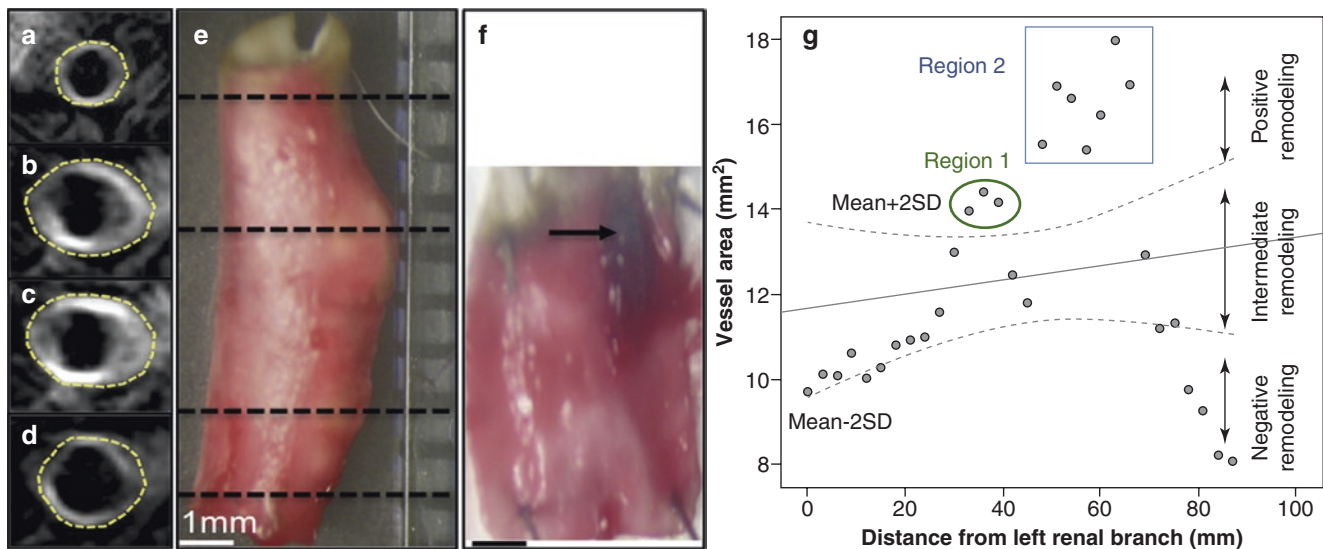


Fig. 14.14 Positive vascular remodeling in disrupted plaques. (a–d) DE MR images obtained after administration of elastin-specific contrast agent show positive remodeling, as defined by enlargement of vessel area (yellow contours). (e) Corresponding *en face* photograph verifies presence of positive vascular remodeling. (f) *En face* photograph of longitudinally open vessel shows thrombus (arrow) attached to vessel wall at proximal end of positive remodeling. (g) Scatterplot

shows change in vessel area measured on consecutive slices along aorta, starting from left renal branch (0 mm) to iliac bifurcation (86 mm). Two regions of the vessel wall underwent positive remodeling, with vessel areas falling above the mean + 2 SD margin. Both plaques disrupted after triggering. Four of seven sections covering the vulnerable region 2 are illustrated in (a–d). (Adapted and reprinted from Phinikaridou et al. [142], © 2014, with permission from RSNA)

Fibrin and Thrombus Formation

Fibrin plays a central role in thrombus formation, but it has been also identified in atherosclerotic lesions of the aorta and coronary arteries [150]. Fibrin I and II are present in several types of atherosclerotic plaque, with fibrin II predominating in later stages and usually colocalizes with macrophages [150]. Although fibrin may enter the intima after mural thrombi originating from plaque rupture or erosion, fragile newly formed vessels may also provide a site of entry [151]. Different fibrin-specific contrast agents have been evaluated in different vascular beds. Gadolinium-based nanoparticles and small peptides (EP-2104R) targeted to fibrin have been successfully used to image atherosclerosis in both animal models and humans [30, 31, 33, 34, 89]. The ability of EP-2104R to detect coronary thrombosis has been first demonstrated in a swine model of intrastent thrombus and has been subsequently successfully translated in a small clinical feasibility study of aortic and carotid thrombosis [19] (Fig. 14.15).

Conclusion

Molecular MR imaging is a promising approach to evaluate biological processes involved in coronary artery disease. This methodology has been successfully validated to

image cellular and structural changes in the vessel wall during atherosclerosis progression in animal models and humans. Coronary vessel wall NCE-MR and CE-MR in patients after myocardial infarction have shown potential for the noninvasive characterization of coronary artery plaque (e.g., endothelial dysfunction, hemorrhage, and fibrosis) without the use of ionizing radiation. For additional characterization of atherosclerotic lesions, target-specific imaging probes have been developed, which allowed successful imaging of extracellular matrix remodeling and coronary thrombosis. In the future, visualization of both early and late biological changes of coronary lesions may allow a more accurate assessment of disease burden and monitoring of the effectiveness of interventions.

Acknowledgments The authors acknowledge financial support from (1) the British Heart Foundation (RG/12/1/29262), (2) the Centre of Excellence in Medical Engineering funded by the Wellcome Trust and EPSRC (WT 088641/Z/09/Z), (3) the British Heart Foundation Centre of Excellence, and (4) the Department of Health via the National Institute for Health Research (NIHR) comprehensive Biomedical Research Centre award to Guy's and St Thomas' NHS Foundation Trust in partnership with King's College London and King's College Hospital NHS Foundation Trust. The views expressed are those of the authors and not necessarily those of the NHS, the NIHR, or the Department of Health.

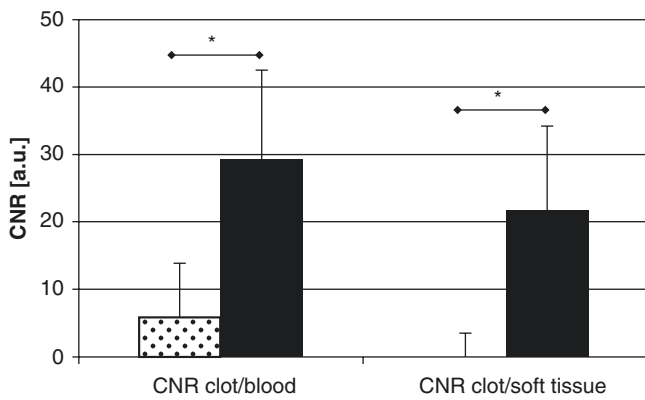
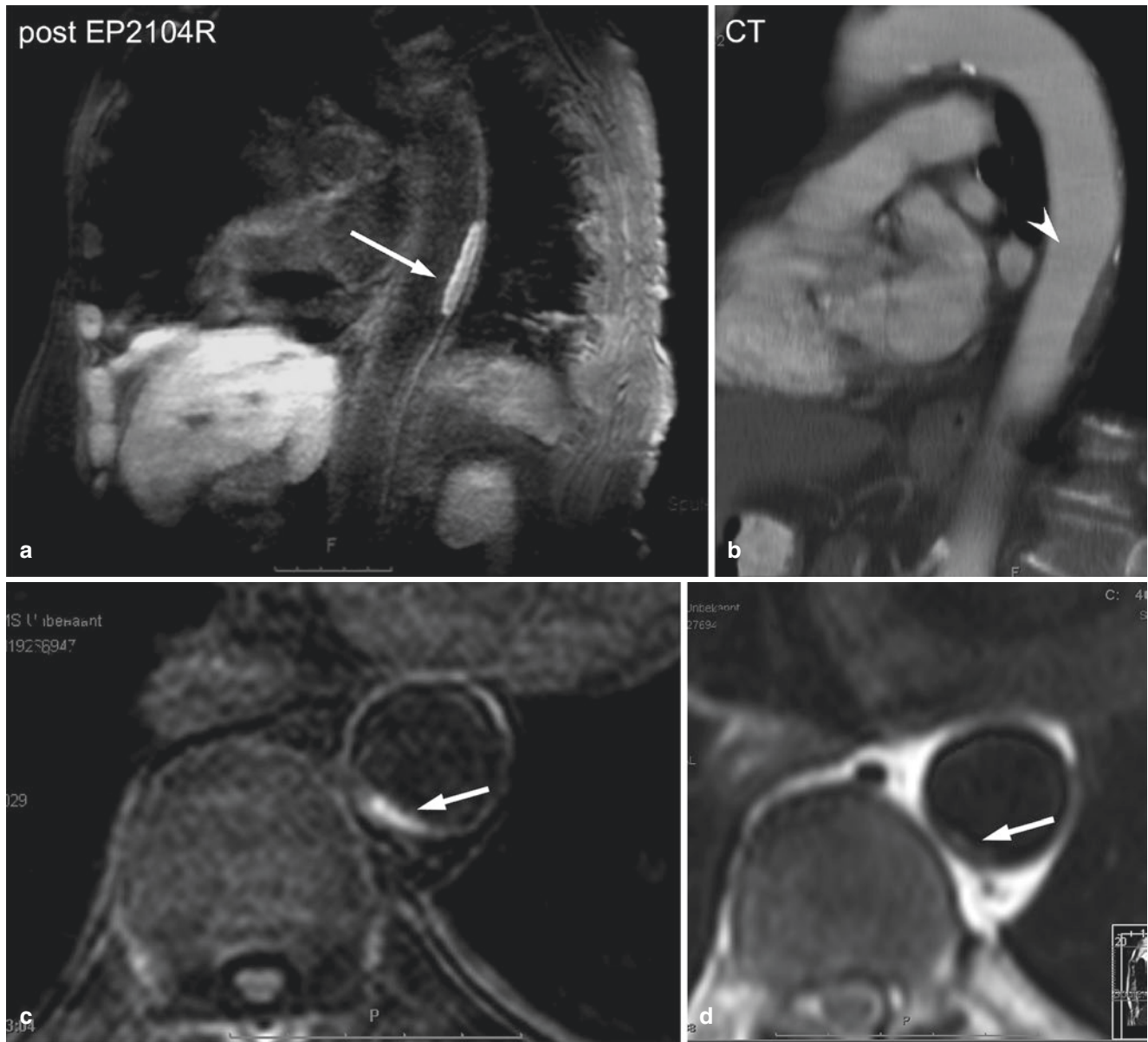


Fig. 14.15 Phase II clinical trial validating clinical feasibility of fibrin-specific MR contrast agent. Human thrombus imaging using EP-2104R, a fibrin-binding contrast agent, in a patient with aortic thrombus. A mural aortic thrombus is well delineated on in-plane post-EP-2104R black-blood MR images (a) while differentiation between thrombus and vessel wall is poor on multi slice CT images (b). Excellent

aortic thrombus visualization on cross-sectional delayed enhancement images post-EP-2104R (c) while differentiation between thrombus and vessel wall is poor on pre-contrast black-blood turbo spin echo (d) MR images. (Adapted and reprinted from Springer, © 2008, Spuentrup et al. [34], Figs. 3, 5, 7, with kind permission from Springer Nature)

References

- Rodgers A, Ezzati M, Vander Hoorn S, Lopez AD, Lin R-B, Murray CJL, Group Comparative Risk Assessment C. Distribution of major health risks: findings from the global burden of disease study. *PLoS Med* 2004;1:e27.
- Ridker PM, Paynter NP, Rifai N, Gaziano JM, Cook NR. C-reactive protein and parental history improve global cardiovascular risk prediction: the Reynolds risk score for men. *Circulation*. 2008;118:2243–51.
- Go AS, Mozaffarian D, Roger VL, Benjamin EJ, Berry JD, Borden WB, et al. Executive summary: heart disease and stroke statistics – 2013 update: a report from the american heart association. *Circulation*. 2013;127:143–52.
- Ambrose JA, Tannenbaum MA, Alexopoulos D, Hjelm Dahl-Monsen CE, Leavy J, Weiss M, et al. Angiographic progression of coronary artery disease and the development of myocardial infarction. *J Am Coll Cardiol*. 1988;12:56–62.
- Varnava AM, Mills PG, Davies MJ. Relationship between coronary artery remodeling and plaque vulnerability. *Circulation*. 2002;105:939–43.
- Glagov S, Weisenberg E, Zarins CK, Stankunavicius R, Kolettis GJ. Compensatory enlargement of human atherosclerotic coronary arteries. *N Engl J Med*. 1987;316:1371–5.
- Ali ZA, Roleder T, Narula J, Mohanty BD, Baber U, Kovacic JC, et al. Increased thin-cap neoatheroma and periprocedural myocardial infarction in drug-eluting stent restenosis: multimodality intravascular imaging of drug-eluting and bare-metal stents. *Circ Cardiovasc Interv*. 2013;6:507–17.
- Madder RD, Wohns DH, Muller JE. Detection by intracoronary near-infrared spectroscopy of lipid core plaque at culprit sites in survivors of cardiac arrest. *J Invasive Cardiol*. 2014;26:78–9.
- de Boer SP, Brugaletta S, Garcia-Garcia HM, Simsek C, Heo JH, Lenzen MJ, et al. Determinants of high cardiovascular risk in relation to plaque-composition of a non-culprit coronary segment visualized by near-infrared spectroscopy in patients undergoing percutaneous coronary intervention. *Eur Heart J*. 2014;35:282–9.
- Wykrzykowska J, Lehman S, Williams G, Parker JA, Palmer MR, Varkey S, et al. Imaging of inflamed and vulnerable plaque in coronary arteries with 18f-fdg pet/ct in patients with suppression of myocardial uptake using a low-carbohydrate, high-fat preparation. *J Nucl Med*. 2009;50:563–8.
- Joshi NV, Vesey AT, Williams MC, Shah AS, Calvert PA, Craighead FH, et al. 18f-fluoride positron emission tomography for identification of ruptured and high-risk coronary atherosclerotic plaques: a prospective clinical trial. *Lancet*. 2014;383:705–13.
- Libby P, Ridker PM, Hansson GK. Progress and challenges in translating the biology of atherosclerosis. *Nature*. 2011;473:317–25.
- Miao C, Chen S, Macedo R, Lai S, Liu K, Li D, Wasserman BA, et al. Positive remodeling of the coronary arteries detected by magnetic resonance imaging in an asymptomatic population: mesa (multi-ethnic study of atherosclerosis). *J Am Coll Cardiol*. 2009;53:1708–15.
- Gerretsen SC, Kooi ME, Kessels AG, Schalla S, Katoh M, van der Geest RJ, et al. Visualization of coronary wall atherosclerosis in asymptomatic subjects and patients with coronary artery disease using magnetic resonance imaging. *PLoS One*. 2010;5:e12998.
- Botnar RM, Buckner A, Kim WY, Viohl I, Gunther RW, Spuentrup E. Initial experiences with in vivo intravascular coronary vessel wall imaging. *J Magn Reson Imaging*. 2003;17:615–9.
- Schar M, Kim WY, Stuber M, Boesiger P, Manning WJ, Botnar RM. The impact of spatial resolution and respiratory motion on MR imaging of atherosclerotic plaque. *J Magn Reson Imaging*. 2003;17:538–44.
- Kim WY, Astrup AS, Stuber M, Tarnow L, Falk E, Botnar RM, et al. Subclinical coronary and aortic atherosclerosis detected by magnetic resonance imaging in type 1 diabetes with and without diabetic nephropathy. *Circulation*. 2007;115:228–35.
- Maintz D, Ozgun M, Hoffmeier A, Fischbach R, Kim WY, Stuber M, et al. Selective coronary artery plaque visualization and differentiation by contrast-enhanced inversion prepared MRI. *Eur Heart J*. 2006;27:1732–6.
- Noguchi T, Kawasaki T, Tanaka A, Yasuda S, Goto Y, Ishihara M, et al. High-intensity signals in coronary plaques on noncontrast t1-weighted magnetic resonance imaging as a novel determinant of coronary events. *J Am Coll Cardiol*. 2014;63(10):989–99.
- Noguchi T, Yamada N, Higashi M, Goto Y, Naito H. High-intensity signals in carotid plaques on t1-weighted magnetic resonance imaging predict coronary events in patients with coronary artery disease. *J Am Coll Cardiol*. 2011;58:416–22.
- Tanaka A, Kawasaki T, Noguchi T, Koga S, Hiramatsu Y, Fukuyama T, Koga N. Hyperintense plaque with noncontrast t1-weighted magnetic resonance coronary plaque imaging leading to acute coronary syndrome. *Circulation*. 2009;120:2400–1.
- Jansen CH, Perera D, Makowski MR, Wiethoff AJ, Phinikaridou A, Razavi RM, et al. Detection of intracoronary thrombus by magnetic resonance imaging in patients with acute myocardial infarction. *Circulation*. 2011;124:416–24.
- Ehara S, Hasegawa T, Nakata S, Matsumoto K, Nishimura S, Iguchi T, et al. Hyperintense plaque identified by magnetic resonance imaging relates to intracoronary thrombus as detected by optical coherence tomography in patients with angina pectoris. *Eur Heart J Cardiovasc Imaging*. 2012;13:394–9.
- Hays AG, Hirsch GA, Kelle S, Gerstenblith G, Weiss RG, Stuber M. Noninvasive visualization of coronary artery endothelial function in healthy subjects and in patients with coronary artery disease. *J Am Coll Cardiol*. 2010;56:1657–65.
- Hays AG, Kelle S, Hirsch GA, Soleimanifard S, Yu J, Agarwal HK, et al. Regional coronary endothelial function is closely related to local early coronary atherosclerosis in patients with mild coronary artery disease: pilot study. *Circ Cardiovasc Imaging*. 2012;5:341–8.
- Hays AG, Stuber M, Hirsch GA, Yu J, Schar M, Weiss RG, Gerstenblith G, Kelle S. Non-invasive detection of coronary endothelial response to sequential handgrip exercise in coronary artery disease patients and healthy adults. *PLoS One*. 2013;8:e58047.
- Kawasaki T, Koga S, Koga N, Noguchi T, Tanaka H, Koga H, et al. Characterization of hyperintense plaque with noncontrast t1-weighted cardiac magnetic resonance coronary plaque imaging-comparison with multislice computed tomography and intravascular ultrasound. *JACC Cardiovasc Imaging*. 2009;2:720–8.
- Yeon SB, Sabir A, Clouse M, Martinezclark PO, Peters DC, Hauser TH, et al. Delayed-enhancement cardiovascular magnetic resonance coronary artery wall imaging: comparison with multislice computed tomography and quantitative coronary angiography. *J Am Coll Cardiol*. 2007;50:441–7.
- Ibrahim T, Makowski MR, Jankauskas A, Maintz D, Karch M, Schachoff S, et al. Serial contrast-enhanced cardiac magnetic resonance imaging demonstrates regression of hyperenhancement within the coronary artery wall in patients after acute myocardial infarction. *JACC Cardiovasc Imaging*. 2009;2:580–8.
- Botnar RM, Buecker A, Wiethoff AJ, Parsons EC Jr, Katoh M, Katsimaglīs G, Weisskoff RM, et al. In vivo magnetic resonance imaging of coronary thrombosis using a fibrin-binding molecular magnetic resonance contrast agent. *Circulation*. 2004;110:1463–6.
- Botnar RM, Perez AS, Witte S, Wiethoff AJ, Laredo J, Hamilton J, et al. In vivo molecular imaging of acute and subacute thrombosis using a fibrin-binding magnetic resonance imaging contrast agent. *Circulation*. 2004;109:2023–9.

32. von Bary C, Makowski M, Preissel A, Keithahn A, Warley A, Spuentrup E, et al. MRI of coronary wall remodeling in a swine model of coronary injury using an elastin-binding contrast agent. *Circ Cardiovasc Imaging*. 2011;4(2):147–55.
33. Vymazal J, Spuentrup E, Cardenas-Molina G, Wiethoff AJ, Hartmann MG, Caravan P, Parsons EC Jr. Thrombus imaging with fibrin-specific gadolinium-based MR contrast agent ep-2104r: results of a phase II clinical study of feasibility. *Investig Radiol*. 2009;44:697–704.
34. Spuentrup E, Botnar RM, Wiethoff A, Ibrahim T, Sebastin K, Katho M, et al. MR imaging of thrombi using ep-2104r, a fibrin specific contrast agent: initial results in patients. *Eur Radiol*. 2008;18(9):1995–2005. (1911)
35. Sato Y, Hatakeyama K, Marutsuka K, Asada Y. Incidence of asymptomatic coronary thrombosis and plaque disruption: comparison of non-cardiac and cardiac deaths among autopsy cases. *Thromb Res*. 2009;124:19–23.
36. Lavin B, Phinikaridou A, Henningson M, Botnar RM. Current development of molecular coronary plaque imaging using magnetic resonance imaging towards clinical application. *Curr Cardiovasc Imaging Rep*. 2014;7(12):9309.
37. Choudhury RP, Fuster V, Fayad ZA. Molecular, cellular and functional imaging of atherothrombosis. *Nat Rev Drug Discov*. 2004;3:913–25.
38. Wilcox JN, Scott NA. Potential role of the adventitia in arteritis and atherosclerosis. *Int J Cardiol*. 1996;54(Suppl):S21–35.
39. Shi Y, O'Brien JE, Fard A, Mannion JD, Wang D, Zalewski A. Adventitial myofibroblasts contribute to neointimal formation in injured porcine coronary arteries. *Circulation*. 1996;94:1655–64.
40. Zhao L, Funk CD. Lipoyxygenase pathways in atherogenesis. *Trends Cardiovasc Med*. 2004;14:191–5.
41. Chiu JJ, Chien S. Effects of disturbed flow on vascular endothelium: pathophysiological basis and clinical perspectives. *Physiol Rev*. 2011;91:327–87.
42. Cines DB, Pollak ES, Buck CA, Loscalzo J, Zimmerman GA, McEver RP, et al. Endothelial cells in physiology and in the pathophysiology of vascular disorders. *Blood*. 1998;91:3527–61.
43. Brodsky SV, Goligorsky MS. Endothelium under stress: local and systemic messages. *Semin Nephrol*. 2012;32:192–8.
44. Galkina E, Ley K. Vascular adhesion molecules in atherosclerosis. *Arterioscler Thromb Vasc Biol*. 2007;27:2292–301.
45. Weber C, Noels H. Atherosclerosis: current pathogenesis and therapeutic options. *Nat Med*. 2011;17:1410–22.
46. Silvestre-Roig C, de Winther MP, Weber C, Daemen MJ, Lutgens E, Soehnlein O. Atherosclerotic plaque destabilization: mechanisms, models, and therapeutic strategies. *Circ Res*. 2014;114:214–26.
47. Falk E. Pathogenesis of atherosclerosis. *J Am Coll Cardiol*. 2006;47(8):C7–12.
48. Narula J, Strauss HW. The popcorn plaques. *Nat Med*. 2007;13(5):532–4.
49. Stone GW, Maehara A, Lansky AJ, de Bruyne B, Cristea E, Mintz GS, et al. Prospect Investigators. A prospective natural-history study of coronary atherosclerosis. *N Engl J Med*. 2011;364:226–35.
50. Narula J, Garg P, Achenbach S, Motoyama S, Virmani R, Strauss HW. Arithmetic of vulnerable plaques for noninvasive imaging. *Nat Clin Pract Cardiovasc Med*. 2008;5(Suppl 2):S2–10.
51. Dabir D, Child N, Kalra A, Rogers T, Gebker R, Jabbour A, et al. Reference values for healthy human myocardium using a T1 mapping methodology: results from the international T1 multicenter cardiovascular magnetic resonance study. *J Cardiovasc Magn Reson*. 2014;16:69.
52. Kawel N, Nacif M, Zavodni A, Jones J, Liu S, Sibley CT, Bluemke DA. T1 mapping of the myocardium: intra-individual assessment of the effect of field strength, cardiac cycle and variation by myocardial region. *J Cardiovasc Magn Reson*. 2012;14:27.
53. Robson MD, Piechnik SK, Tunnicliffe EM, Neubauer S. T measurements in the human myocardium: the effects of magnetization transfer on the sasha and molli sequences. *Magn Reson Med*. 2013;70(3):664–70.
54. Salerno M, Janardhanan R, Jiji RS, Brooks J, Adenaw N, Mehta B, et al. Comparison of methods for determining the partition coefficient of gadolinium in the myocardium using T1 mapping. *J Magn Reson Imaging*. 2013;38:217–24.
55. Ichikawa Y, Sakuma H, Suzawa N, Kitagawa K, Makino K, Hirano T, Takeda K. Late gadolinium-enhanced magnetic resonance imaging in acute and chronic myocardial infarction. Improved prediction of regional myocardial contraction in the chronic state by measuring thickness of nonenhanced myocardium. *J Am Coll Cardiol*. 2005;45:901–9.
56. Nitz WR, Reimer P. Contrast mechanisms in MR imaging. *Eur Radiol*. 1999;9:1032–46.
57. Keegan J, Gatehouse PD, Yang GZ, Firmin DN. Non-model-based correction of respiratory motion using beat-to-beat 3d spiral fat-selective imaging. *J Magn Reson Imaging*. 2007;26:624–9.
58. Dixon WT. Simple proton spectroscopic imaging. *Radiology*. 1984;153:189–94.
59. Glover GH, Schneider E. Three-point Dixon technique for true water/fat decomposition with B0 inhomogeneity correction. *Magn Reson Med*. 1991;18:371–83.
60. Fayad ZA, Fuster V, Fallon JT, Jayasundera T, Worthley SG, Helft G, et al. Noninvasive in vivo human coronary artery lumen and wall imaging using black-blood magnetic resonance imaging. *Circulation*. 2000;102:506–10.
61. Botnar RM, Stuber M, Kissinger KV, Kim WY, Spuentrup E, Manning WJ. Noninvasive coronary vessel wall and plaque imaging with magnetic resonance imaging. *Circulation*. 2000;102:2582–7.
62. Botnar RM, Kim WY, Bornert P, Stuber M, Spuentrup E, Manning WJ. 3d coronary vessel wall imaging utilizing a local inversion technique with spiral image acquisition. *Magn Reson Med*. 2001;46:848–54.
63. Wang J, Yarnykh VL, Hatsukami T, Chu B, Balu N, Yuan C. Improved suppression of plaque-mimicking artifacts in black-blood carotid atherosclerosis imaging using a multislice motion-sensitized driven-equilibrium (msde) turbo spin-echo (tse) sequence. *Magn Reson Med*. 2007;58:973–81.
64. Li L, Miller KL, Jezzard P. Dante-prepared pulse trains: a novel approach to motion-sensitized and motion-suppressed quantitative magnetic resonance imaging. *Magn Reson Med*. 2012;68:1423–38.
65. Fan Z, Zhang Z, Chung YC, Weale P, Zuehlsdorff S, Carr J, Li D. Carotid arterial wall MRI at 3T using 3D variable-flip-angle turbo spin-echo (tse) with flow-sensitive dephasing (fsd). *J Magn Reson Imaging*. 2010;31:645–54.
66. Oei ML, Ozgun M, Seifarth H, Bunck A, Fischbach R, Orwat S, et al. T1-weighted MRI for the detection of coronary artery plaque haemorrhage. *Eur Radiol*. 2010;20:2817–23.
67. Andia ME, Henningson M, Hussain T, Phinikaridou A, Protti A, Greil G, Botnar RM. Flow-independent 3d whole-heart vessel wall imaging using an interleaved T2-preparation acquisition. *Magn Reson Med*. 2013;69(1):150–7.
68. Xie J, Bi X, Fan Z, Bhat H, Shah S, Zuehlsdorff S, Li D. 3d flow-independent peripheral vessel wall imaging using T2-prepared phase-sensitive inversion-recovery steady-state free precession. *J Magn Reson Imaging*. 2010;32:399–408.
69. Messroghli DR, Radjenovic A, Kozierke S, Higgins DM, Sivanathan MU, Ridgway JP. Modified look-locker inversion recovery (molli) for high-resolution T1 mapping of the heart. *Magn Reson Med*. 2004;52:141–6.

70. Chow K, Flewitt JA, Green JD, Pagano JJ, Friedrich MG, Thompson RB. Saturation recovery single-shot acquisition (sasha) for myocardial t(1) mapping. *Magn Reson Med*. 2014;71:2082–95.
71. Roujol S, Weingartner S, Foppa M, Chow K, Kawaji K, Ngo LH, et al. Accuracy, precision, and reproducibility of four t1 mapping sequences: a head-to-head comparison of molli, shmollo, sasha, and sapphire. *Radiology*. 2014;272:683–9.
72. van Heeswijk RB, Piccini D, Feliciano H, Hullin R, Schwitter J, Stuber M. Self-navigated isotropic three-dimensional cardiac t mapping. *Magn Reson Med*. 2015;73(4):1549–54.
73. van Heeswijk RB, Feliciano H, Bongard C, Bonanno G, Coppo S, Lauriers N, et al. Free-breathing 3 t magnetic resonance t2-mapping of the heart. *JACC Cardiovasc Imaging*. 2012;5:1231–9.
74. Ding H, Fernandez-de-Manuel L, Schar M, Schuleri KH, Halperin H, He L, et al. Three-dimensional whole-heart t mapping at 3t. *Magn Reson Med*. 2015;74(3):803–16.
75. Henningsson M, Koken P, Stehning C, Razavi R, Prieto C, Botnar RM. Whole-heart coronary MR angiography with 2d self-navigated image reconstruction. *Magn Reson Med*. 2012;67:437–45.
76. Stehning C, Bornert P, Nehrke K, Eggers H, Stuber M. Free-breathing whole-heart coronary MRA with 3d radial ssfp and self-navigated image reconstruction. *Magn Reson Med*. 2005;54:476–80.
77. Prieto C, Doneva M, Usman M, Henningsson M, Greil G, Schaeffter T, Botnar RM. Highly efficient respiratory motion compensated free-breathing coronary MRA using golden-step cartesian acquisition. *J Magn Reson Imaging*. 2015;41:738–46.
78. Pang J, Bhat H, Sharif B, Fan Z, Thomson LE, LaBounty T, et al. Whole-heart coronary MRA with 100% respiratory gating efficiency: self-navigated three-dimensional retrospective image-based motion correction (trim). *Magn Reson Med*. 2014;71:67–74.
79. Henningsson M, Prieto C, Chiribiri A, Vaillant G, Razavi R, Botnar RM. Whole-heart coronary MRA with 3d affine motion correction using 3d image-based navigation. *Magn Reson Med*. 2014;71:173–81.
80. Aitken AP, Henningsson M, Botnar RM, Schaeffter T, Prieto C. 100% efficient three-dimensional coronary MR angiography with two-dimensional beat-to-beat translational and bin-to-bin affine motion correction. *Magn Reson Med*. 2015;74:756–64.
81. Pang J, Sharif B, Fan Z, Bi X, Arsanjani R, Berman DS, Li D. Ecg and navigator-free four-dimensional whole-heart coronary MRA for simultaneous visualization of cardiac anatomy and function. *Magn Reson Med*. 2014;72:1208–17.
82. Coppo S, Piccini D, Bonanno G, Chaptinel J, Vincenti G, Feliciano H, et al. Free-running 4d whole-heart self-navigated golden angle MRI: initial results. *Magn Reson Med*. 2015;74(5):1306–16.
83. Caravan P. Strategies for increasing the sensitivity of gadolinium based MRI contrast agents. *Chem Soc Rev*. 2006;35:512.
84. Calcagno C, Ramachandran S, Izquierdo-Garcia D, Mani V, Millon A, Rosenbaum D, Tawakol A, et al. The complementary roles of dynamic contrast-enhanced MRI and 18f-fluorodeoxyglucose pet/ct for imaging of carotid atherosclerosis. *Eur J Nucl Med Mol Imaging*. 2013;40:1884–93.
85. Caravan P, Ellison JJ, McMurry TJ, Lauffer RB. Gadolinium(iii) chelates as MRI contrast agents: structure, dynamics, and applications. *Chem Rev*. 1999;99:2293–352.
86. Caravan P, Cloutier NJ, Greenfield MT, McDermid SA, Dunham SU, Bulte JW, et al. The interaction of ms-325 with human serum albumin and its effect on proton relaxation rates. *J Am Chem Soc*. 2002;124:3152–62.
87. Nivorozhkin AL, Kolodziej AF, Caravan P, Greenfield MT, Lauffer RB, McMurry TJ. Enzyme-activated gd(3+) magnetic resonance imaging contrast agents with a proton receptor-induced magnetization enhancement. *Angew Chem Int Ed Engl*. 2001;40:2903–6.
88. Makowski MR, Wiethoff AJ, Blume U, Cuello F, Warley A, Jansen CH, et al. Assessment of atherosclerotic plaque burden with an elastin-specific magnetic resonance contrast agent. *Nat Med*. 2011;17:383–8.
89. Andia ME, Saha P, Jenkins J, Modarai B, Wiethoff AJ, Phinikaridou A, Grover SP, et al. Fibrin-targeted magnetic resonance imaging allows in vivo quantification of thrombus fibrin content and identifies thrombi amenable for thrombolysis. *Arterioscler Thromb Vasc Biol*. 2014;34:1193–8.
90. Flacke S, Fischer S, Scott MJ, Fuhrhop RJ, Allen JS, McLean M, et al. Novel MRI contrast agent for molecular imaging of fibrin: implications for detecting vulnerable plaques. *Circulation*. 2001;104:1280–5.
91. Winter PM, Morawski AM, Caruthers SD, Fuhrhop RW, Zhang H, Williams TA, et al. Molecular imaging of angiogenesis in early-stage atherosclerosis with alpha(v)beta3-integrin-targeted nanoparticles. *Circulation*. 2003;108:2270–4.
92. Weinmann HJ, Brasch RC, Press WR, Wesbey GE. Characteristics of gadolinium-dtpa complex: a potential nmr contrast agent. *AJR Am J Roentgenol*. 1984;142:619–24.
93. Laniado M, Weinmann HJ, Schorner W, Felix R, Speck U. First use of gddtpa/dimeglumine in man. *Physiol Chem Phys Med NMR*. 1984;16:157–65.
94. Weissleder R, Elizondo G, Wittenberg J, Rabito CA, Bengel HH, Josephson L. Ultrasmall superparamagnetic iron oxide: characterization of a new class of contrast agents for MR imaging. *Radiology*. 1990;175:489–93.
95. Farrar CT, Dai G, Novikov M, Rosenzweig A, Weissleder R, Rosen BR, Sosnovik DE. Impact of field strength and iron oxide nanoparticle concentration on the linearity and diagnostic accuracy of off-resonance imaging. *NMR Biomed*. 2008;21:453–63.
96. Wang YX, Xuan S, Port M, Idee JM. Recent advances in superparamagnetic iron oxide nanoparticles for cellular imaging and targeted therapy research. *Curr Pharm Des*. 2013;19:6575–93.
97. Tang TY, Muller KH, Graves MJ, Li ZY, Walsh SR, Young V, et al. Iron oxide particles for atheroma imaging. *Arterioscler Thromb Vasc Biol*. 2009;29:1001–8.
98. Segers FM, den Adel B, Bot I, van der Graaf LM, van der Veer EP, Gonzalez W, et al. Scavenger receptor-ai-targeted iron oxide nanoparticles for in vivo MRI detection of atherosclerotic lesions. *Arterioscler Thromb Vasc Biol*. 2013;33:1812–9.
99. Yilmaz A, Rosch S, Klingel K, Kandolf R, Helluy X, Hiller KH, et al. Magnetic resonance imaging (MRI) of inflamed myocardium using iron oxide nanoparticles in patients with acute myocardial infarction – preliminary results. *Int J Cardiol*. 2013;163:175–82.
100. Islam T, Harisinghani MG. Overview of nanoparticle use in cancer imaging. *Cancer Biomark*. 2009;5:61–7.
101. Briley-Saebo KC, Shaw PX, Mulder WJ, Choi SH, Vucic E, Aguinaldo JG, et al. Targeted molecular probes for imaging atherosclerotic lesions with magnetic resonance using antibodies that recognize oxidation-specific epitopes. *Circulation*. 2008;117:3206–15.
102. Amirbekian V, Lipinski MJ, Briley-Saebo KC, Amirbekian S, Aguinaldo JG, Weinreb DB, et al. Detecting and assessing macrophages in vivo to evaluate atherosclerosis noninvasively using molecular MRI. *Proc Natl Acad Sci U S A*. 2007;104:961–6.
103. Ruehm SG, Corot C, Vogt P, Kolb S, Debatin JF. Magnetic resonance imaging of atherosclerotic plaque with ultrasmall superparamagnetic particles of iron oxide in hyperlipidemic rabbits. *Circulation*. 2001;103:415–22.
104. Kooi ME, Cappendijk VC, Cleutjens KBJM, Kessels AGH, Kitslaar PJEHM, Borgers M, et al. Accumulation of ultrasmall superparamagnetic particles of iron oxide in human atherosclerotic plaques can be detected by in vivo magnetic resonance imaging. *Circulation*. 2003;107:2453–8.

105. Tang TY, Howarth SP, Miller SR, Graves MJ, U-King-Im JM, Li ZY, et al. Correlation of carotid atheromatous plaque inflammation using uspio-enhanced MR imaging with degree of luminal stenosis. *Stroke*. 2008;39:2144–7.
106. Tang TY, Howarth SP, Miller SR, Graves MJ, U-King-Im JM, Li ZY, et al. Comparison of the inflammatory burden of truly asymptomatic carotid atheroma with atherosclerotic plaques in patients with asymptomatic carotid stenosis undergoing coronary artery bypass grafting: an ultrasmall superparamagnetic iron oxide enhanced magnetic resonance study. *Eur J Vasc Endovasc Surg*. 2008;35:392–8.
107. Phinikaridou A, Andia ME, Protti A, Indermuehle A, Shah A, Smith A, Warley A, Botnar RM. Noninvasive magnetic resonance imaging evaluation of endothelial permeability in murine atherosclerosis using an albumin-binding contrast agent. *Circulation*. 2012;126(6):707–19.
108. Phinikaridou A, Andia ME, Passacuale G, Ferro A, Botnar RM. Noninvasive MRI monitoring of the effect of interventions on endothelial permeability in murine atherosclerosis using an albumin-binding contrast agent. *J Am Heart Assoc*. 2013;2:e000402.
109. Lobbes MB, Heeneman S, Passos VL, Welten R, Kwee RM, van der Geest RJ, et al. Gadofosveset-enhanced magnetic resonance imaging of human carotid atherosclerotic plaques: a proof-of-concept study. *Investig Radiol*. 2010;45(5):275–81.
110. Lobbes MB, Miserus RJ, Heeneman S, Passos VL, Mutsaers PH, Debernardi N, et al. Atherosclerosis: contrast-enhanced MR imaging of vessel wall in rabbit model – comparison of gadofosveset and gadopentetate dimeglumine. *Radiology*. 2009;250:682–91.
111. Pedersen SF, Thrysoe SA, Paaske WP, Thim T, Falk E, Ringgaard S, Kim WY. CMR assessment of endothelial damage and angiogenesis in porcine coronary arteries using gadofosveset. *J Cardiovasc Magn Reson*. 2011;13:10.
112. McAteer MA, Schneider JE, Ali ZA, Warrick N, Bursill CA, von zur Muhlen C, et al. Magnetic resonance imaging of endothelial adhesion molecules in mouse atherosclerosis using dual-targeted microparticles of iron oxide. *Arterioscler Thromb Vasc Biol*. 2008;28:77–83.
113. Nahrendorf M, Jaffer FA, Kelly KA, Sosnovik DE, Aikawa E, Libby P, Weissleder R. Noninvasive vascular cell adhesion molecule-1 imaging identifies inflammatory activation of cells in atherosclerosis. *Circulation*. 2006;114:1504–11.
114. Sluimer JC, Kolodgie FD, Bijmens AP, Maxfield K, Pacheco E, Kutys B, et al. Thin-walled microvessels in human coronary atherosclerotic plaques show incomplete endothelial junctions relevance of compromised structural integrity for intraplaque microvascular leakage. *J Am Coll Cardiol*. 2009;53:1517–27.
115. Kolodgie FD, Narula J, Yuan C, Burke AP, Finn AV, Virmani R. Elimination of neoangiogenesis for plaque stabilization: is there a role for local drug therapy? *J Am Coll Cardiol*. 2007;49:2093–101.
116. Russell DA, Abbott CR, Gough MJ. Vascular endothelial growth factor is associated with histological instability of carotid plaques. *Br J Surg*. 2008;95:576–81.
117. Virmani R, Kolodgie FD, Burke AP, Finn AV, Gold HK, Tulenko TN, Wrenn SP, Narula J. Atherosclerotic plaque progression and vulnerability to rupture: angiogenesis as a source of intraplaque hemorrhage. *Arterioscler Thromb Vasc Biol*. 2005;25:2054–61.
118. Manduteanu I, Simionescu M. Inflammation in atherosclerosis: a cause or a result of vascular disorders? *J Cell Mol Med*. 2012;16:1978–90.
119. Purushothaman KR, Sanz J, Zias E, Fuster V, Moreno PR. Atherosclerosis neovascularization and imaging. *Curr Mol Med*. 2006;6:549–56.
120. Kerwin WS, O'Brien KD, Ferguson MS, Polissar N, Hatsukami TS, Yuan C. Inflammation in carotid atherosclerotic plaque: a dynamic contrast-enhanced MR imaging study. *Radiology*. 2006;241:459–68.
121. Jaffer FA, Nahrendorf M, Sosnovik D, Kelly KA, Aikawa E, Weissleder R. Cellular imaging of inflammation in atherosclerosis using magnetofluorescent nanomaterials. *Mol Imaging*. 2006;5:85–92.
122. Tait JF. Imaging of apoptosis. *J Nucl Med*. 2008;49:1573–6.
123. van Tilborg GA, Vucic E, Strijkers GJ, Cormode DP, Mani V, Skajaa T, et al. Annexin a5-functionalized bimodal nanoparticles for MRI and fluorescence imaging of atherosclerotic plaques. *Bioconjug Chem*. 2010;21:1794–803.
124. Ye D, Shuhendler AJ, Cui L, Tong L, Tee SS, Tikhomirov G, et al. Bioorthogonal cyclization-mediated in situ self-assembly of small-molecule probes for imaging caspase activity in vivo. *Nat Chem*. 2014;6:519–26.
125. Pello OM, Silvestre C, De Pizzol M, Andres V. A glimpse on the phenomenon of macrophage polarization during atherosclerosis. *Immunobiology*. 2011;216:1172–6.
126. Durand E, Raynaud JS, Bruneval P, Brigger I, Al Haj Zen A, et al. Magnetic resonance imaging of ruptured plaques in the rabbit with ultrasmall superparamagnetic particles of iron oxide. *J Vasc Res*. 2007;44:119–28.
127. Morishige K, Kacher DF, Libby P, Josephson L, Ganz P, Weissleder R, Aikawa M. High-resolution magnetic resonance imaging enhanced with superparamagnetic nanoparticles measures macrophage burden in atherosclerosis. *Circulation*. 2010;122:1707–15.
128. Schmitz SA, Coupland SE, Gust R, Winterhalter S, Wagner S, Kresse M, et al. Superparamagnetic iron oxide-enhanced MRI of atherosclerotic plaques in watanabe heritable hyperlipidemic rabbits. *Investig Radiol*. 2000;35:460–71.
129. Sigovan M, Boussel L, Sulaiman A, Sappey-Marini D, Alsaid H, Desbleds-Mansard C, et al. Rapid-clearance iron nanoparticles for inflammation imaging of atherosclerotic plaque: initial experience in animal model. *Radiology*. 2009;252:401–9.
130. Smith BR, Heverhagen J, Knopp M, Schmalbrock P, Shapiro J, Shiomi M, et al. Localization to atherosclerotic plaque and bio-distribution of biochemically derivatized superparamagnetic iron oxide nanoparticles (spions) contrast particles for magnetic resonance imaging (MRI). *Biomed Microdevices*. 2007;9:719–27.
131. Makowski MR, Varma G, Wiethoff AJ, Smith A, Mattock K, Jansen CH, et al. Noninvasive assessment of atherosclerotic plaque progression in apoe^{-/-} mice using susceptibility gradient mapping. *Circ Cardiovasc Imaging*. 2011;4(3):295–303.
132. Tang TY, Patterson AJ, Miller SR, Graves MJ, Howarth SPS, U-King-Im JM, et al. Temporal dependence of in vivo uspio-enhanced MRI signal changes in human carotid atheromatous plaques. *Neuroradiology*. 2009;51:457–65.
133. Tang TY, Howarth SP, Miller SR, Graves MJ, U-King-Im JM, Trivedi RA, et al. Comparison of the inflammatory burden of truly asymptomatic carotid atheroma with atherosclerotic plaques contralateral to symptomatic carotid stenosis: an ultra small superparamagnetic iron oxide enhanced magnetic resonance study. *J Neurol Neurosurg Psychiatry*. 2007;78:1337–43.
134. Tang TY, Howarth SP, Li ZY, Miller SR, Graves MJ, U-King-Im JM, et al. Correlation of carotid atheromatous plaque inflammation with biomechanical stress: utility of uspio enhanced MR imaging and finite element analysis. *Atherosclerosis*. 2008;196:879–87.
135. Trivedi RA, Mallawarachi C, U-King-Im J-M, Graves MJ, Horsley J, Goddard MJ, et al. Identifying inflamed carotid plaques using in vivo uspio-enhanced MR imaging to label plaque macrophages. *Arterioscler Thromb Vasc Biol*. 2006;26:1601–6.
136. Fogel U, Ding Z, Hardung H, Jander S, Reichmann G, Jacoby C, Schubert R, Schrader J. In vivo monitoring of inflammation after cardiac and cerebral ischemia by fluorine magnetic resonance imaging. *Circulation*. 2008;118:140–8.

137. Burnett JR. Lipids, lipoproteins, atherosclerosis and cardiovascular disease. *Clin Biochem Rev.* 2004;25:2.
138. Sirol M, Itskovich VV, Mani V, Aguinaldo JG, Fallon JT, Misselwitz B, et al. Lipid-rich atherosclerotic plaques detected by gadofluorine-enhanced in vivo magnetic resonance imaging. *Circulation.* 2004;109:2890–6.
139. Chen W, Vucic E, Leupold E, Mulder WJ, Cormode DP, Briley-Saebo KC, et al. Incorporation of an apoe-derived lipopeptide in high-density lipoprotein MRI contrast agents for enhanced imaging of macrophages in atherosclerosis. *Contrast Media Mol Imaging.* 2008;3:233–42.
140. Katsuda S, Kaji T. Atherosclerosis and extracellular matrix. *J Atheroscler Thromb.* 2003;10:267–74.
141. Makowski MR, Preissel A, von Bary C, Warley A, Schachoff S, Keithan A, et al. Three-dimensional imaging of the aortic vessel wall using an elastin-specific magnetic resonance contrast agent. *Investig Radiol.* 2012;47:438–44.
142. Phinikaridou A, Andia ME, Indermuehle A, Onthank DC, Cesati RR, Smith A, et al. Vascular remodeling and plaque vulnerability in a rabbit model of atherosclerosis: comparison of delayed-enhancement MR imaging with an elastin-specific contrast agent and unenhanced black-blood MR imaging. *Radiology.* 2014;271:390–9.
143. Motoyama S, Kondo T, Sarai M, Sugiura A, Harigaya H, Sato T, et al. Multislice computed tomographic characteristics of coronary lesions in acute coronary syndromes. *J Am Coll Cardiol.* 2007;50:319–26.
144. Motoyama S, Sarai M, Harigaya H, Anno H, Inoue K, Hara T, et al. Computed tomographic angiography characteristics of atherosclerotic plaques subsequently resulting in acute coronary syndrome. *J Am Coll Cardiol.* 2009;54:49–57.
145. Gough PJ, Gomez IG, Wille PT, Raines EW. Macrophage expression of active mmp-9 induces acute plaque disruption in apoe-deficient mice. *J Clin Invest.* 2006;116:59–69.
146. Lancelot E, Amirbekian V, Brigger I, Raynaud JS, Ballet S, David C, et al. Evaluation of matrix metalloproteinases in atherosclerosis using a novel noninvasive imaging approach. *Arterioscler Thromb Vasc Biol.* 2008;28:425–32.
147. Hyafil F, Vucic E, Cornily JC, Sharma R, Amirbekian V, Blackwell F, et al. Monitoring of arterial wall remodelling in atherosclerotic rabbits with a magnetic resonance imaging contrast agent binding to matrix metalloproteinases. *Eur Heart J.* 2011;32:1561–71.
148. Nicholls SJ, Hazen SL. Myeloperoxidase and cardiovascular disease. *Arterioscler Thromb Vasc Biol.* 2005;25:1102–11.
149. Ronald JA, Chen JW, Chen Y, Hamilton AM, Rodriguez E, Reynolds F, et al. Enzyme-sensitive magnetic resonance imaging targeting myeloperoxidase identifies active inflammation in experimental rabbit atherosclerotic plaques. *Circulation.* 2009;120:592–9.
150. Tavora F, Cresswell N, Li L, Ripple M, Burke A. Immunolocalisation of fibrin in coronary atherosclerosis: implications for necrotic core development. *Pathology.* 2010;42:15–22.
151. Falk E, Shah PK, Fuster V. Coronary plaque disruption. *Circulation.* 1995;92:657–71.